Icarus 311 (2018) 52–68

Contents lists available at ScienceDirect

Icarus

journal homepage: www.elsevier.com/locate/icarus

Hypervelocity impact fragmentation of basalt and shale projectiles

J.E. Wickham-Eade, M.J. Burchell*, M.C. Price, K.H. Harriss

Centre for Astronomy and Planetary Sciences, School of Physical Sciences, Ingram Building, University of Kent, Canterbury, Kent CT2 7NH, United Kingdom

ARTICLE INFO

Article history:
Received 11 July 2017
Revised 12 March 2018
Accepted 15 March 2018
Available online 16 March 2018

Keywords:
Impact processes
Moon
Asteroid Ceres
Asteroid Vesta
Pluto

ABSTRACT

Results are presented for the fragmentation of projectiles in laboratory experiments. 1.5 mm cubes and spheres of basalt and shale were impacted onto water at normal incidence and speeds from 0.39 to 6.13 km s^{-1}; corresponding to peak shock pressures 0.7–32 GPa. Projectile fragments were collected and measured (over 100,000 fragments in some impacts, at sizes down to 10 μm). Power laws were fitted to the cumulative fragment size distributions and the evolution of the exponent vs. impact speed and peak shock pressure found. The gradient of each of these power laws increased with increasing impact speed/peak shock pressure. The percentage of the projectiles recovered in the impacts was found and used to estimate projectile remnant survival in different solar system impact scenarios at the mean impact speed appropriate to that scenario. For Pluto, the Moon and in the asteroid belt approximately 55%, 40% and 15%, respectively, of an impactor could survive and be recovered at an impact site. Finally, the catastrophic disruption energy densities of basalt and shale were measured and found to be 24×10^4 J kg^{-1} and 9×10^4 J kg^{-1}, respectively, a factor of ~2.5 difference. These corresponded to peak shock pressures of 1 to 1.5 GPa (basalt), and 0.8 GPa (shale). This is for near normal-incidence impacts where tensile strength is dominant. For shallow angle impacts we suggest shear effects dominate, resulting in lower critical energy densities and peak shock pressures. We also determine a method to ascertain information about fragment sizes in solar system impact events using a known size of impactor. The results are used to predict projectile fragments sizes for the Veneneia and Rheasilvia crater forming impacts on Vesta, and similar impacts on Ceres.

1. Introduction

Impacts in excess of a few km s^{-1} are deemed hypervelocity impacts, and have long been studied as a major evolution process for solar system bodies and surfaces. Here on Earth the mean impact speed is usually given as around 20 km s^{-1} (Steel, 1998; Jeffers et al., 2001). However, the mean speed of impacts varies depending on their location within the Solar System. For example, the mean impact speed in the asteroid belt is approximately 5 km s^{-1} (Bottke et al., 1994), with the exact speed depending on the exact conditions, e.g. the mean impact speed on Vesta is estimated as 4.75 km s^{-1} (Reddy et al., 2012). Lower impact speeds (0.5–1 km s^{-1}) are expected for Kuiper Belt objects in the outer Solar System (Zahnle et al., 2003). However, if a body is a satellite of a planet, there will also be a contribution to the mean impact speed from the gravitational attraction of the larger nearby planet. Hence the satellites of Jupiter and Saturn will have mean impact speeds that increase the closer they are to the parent planet (e.g., see Zahne et al., 2003; Burchell et al., 2005). There are even more specific, niche examples, of impacts, such as that of terrestrial material ejected after impacts on Earth, which then impacts the Moon. Such impacts have speed ranges which need to be found for that specific example (e.g., see Armstrong, 2010, who gives the mode speed for terrestrial ejecta on the Moon as approximately 2.8 km s^{-1}).

There has been significant research into impact cratering events and the resulting ejecta. A typical recent summary of impact related research can be found in Osinski and Pierazzo (2013) and references therein. What is sometimes overlooked however is that projectile material itself may survive the impact (albeit in modified and/or heavily fragmented form). There has long been discussion of this, albeit less than that for other aspects of impacts. For example, early work by Gault and Heitowit (1963) looked to see how the kinetic energy of the projectile was partitioned during an impact, and estimated that the projectile internal energy (the waste heat) was 6% (of the projectile's kinetic energy) for sand and between 4% and 12% for basalt. Later, Gault and Wedekind (1978) discussed projectile ricochet in shallow angle impacts in the laboratory, as well as the energy density (Q_p^*) needed to fragment alu-

* Corresponding author.
E-mail address: m.j.burchell@kent.ac.uk (M.J. Burchell).

https://doi.org/10.1016/j.icarus.2018.03.017

minium and basalt projectiles in an impact. Note that this concept of Q_p^* is similar to that of the critical energy density needed in an impact to disrupt a target (Q^*). Thus it is the energy density (kinetic energy divided by mass) which, on average, results in the largest surviving fragment possessing half the original mass of the parent body (here the projectile). The presence of the subscript p indicates that the projectile alone is being considered, and thus $Q_p^* = \frac{1}{2}v^2$. This approach is extended in Schultz and Gault (1990a), who considered in detail the break-up of projectiles in such impacts. In that work, Schultz and Gault reported firing aluminium and basalt spheres at targets of mostly steel, but with examples of water and aluminium targets as well. The impacts covered a speed range of 0.4 to 5.3 km s^{-1}, and were at very shallow angles of incidence (30° from the horizontal or less). Projectile disruption was reported, with significant fragments of the impactor recovered post-shot (over 50% in some cases). Where projectile ricochet was reported, in some cases the incident projectile was effectively intact after the impact. Studies of shallow angle ricochet have also been reported for basalt targets covered with sand (Burchell et al., 2010, 2015). As well as observing intact ricochet, they also reported very little reduction in outgoing speed compared to the incident speed. Separate studies have also considered projectile fragmentation during penetration of thin plates (e.g. Piekutowski, 1995). Schultz and Gault (1984) also considered how projectile fragmentation can influence crater morphology. They showed that when the impact induced shock pressures exceeded the dynamic strength of the projectile, cratering efficiency was reduced. Since this occurs at modest impact speeds (less than a few km s^{-1}), extrapolation of low speed data to higher speed examples in the Solar System may not be effective.

Previous work in the laboratory which has observed projectile fragmentation also includes impacts into metal targets at speeds of up to 5 or 6 km s^{-1} (which can involve shock pressures of 80 to over 100 GPa). Examples of this include Hernandez et al. (2006) for metal projectiles, and Burchell et al. (2008) for mineralic impactors. Despite the extreme shocks, in the latter example, post-impact fragments of the mineral projectiles retained sufficient internal structure to have recognisable Raman spectra. Recently, studies of Raman spectra from olivine grains after impacts at speeds up to 6 km s^{-1}, do however show some subtle changes in peak positions. This suggests that some fine changes in structure may be occurring due to the shock during impact (Foster et al., 2013; Harriss and Burchell, 2016).

In addition, Nagaoka et al. (2014) fired millimetre-sized pyrophyllite and basalt projectiles onto regolith-like sand targets at velocities up to 960 m s^{-1}. They determined Q_p^* to be $(4.5 \pm 1.1) \times 10^4$ for pyrophyllite and $(9.0 \pm 1.9) \times 10^4$ J kg^{-1} for basalt projectiles (Nagaoka et al., 2014). They also found that destruction of rock projectiles occurred when the peak pressure was approximately ten times the tensile strength of the rocks (Nagaoka et al., 2014). Recently, Avdellidou et al. (2016) fired forsterite olivine and synthetic basalt projectiles onto low porosity ($< 10\%$) pure water–ice targets at speeds between 0.38 and 3.50 km s^{-1}. From this, the estimated implanted mass on the target body was found to be a few percent of the initial projectile mass. Furthermore, they found an order of magnitude difference for Q_p^*, between the olivine ($Q_p^* = 7.07 \times 10^5$ J kg^{-1}) and basalt ($Q_p^* = 2.31 \times 10^6$ J kg^{-1}). However, they found that the two projectile materials had very similar fragment size frequency distributions (Avdellidou et al., 2016).

As well as laboratory experiments, there is extensive evidence for projectile survival in Solar System impact events. For example, projectile fragments have been recovered at 13 terrestrial impact sites including Barringer, Morokweng and Chicxulub craters (see Table 15.1, Goderis et al., 2013, and references therein). Furthermore, analysis of Apollo era lunar samples shows that projectile fragments from impacts early in the Moon's history can be found within the lunar regolith (e.g. Joy et al., 2012, and references therein). Schultz and Crawford (2016) have suggested that the high meteoritic component found in samples returned from the Apollo 16 landing site may arise from ejecta from the impact which formed the Imbrium basin on the Moon. As well as projectile material being mixed within the lunar regolith, Yue et al. (2013) used numerical models to show that for vertical impact velocities below 12 km s^{-1}, projectile material may survive the impact and be found in the central peak of the final crater. There are also suggestions by Reddy et al. (2012) that the dark material on Asteroid (4) Vesta could be of exogenic origin. This is based on the observation that the majority of spectra of the dark material are similar to carbonaceous chondrite meteorites, indicating mixing of such impactors with materials indigenous to Vesta. Relating to this observation, Daly and Schultz (2013, 2014, 2015a, 2015b, 2016) have conducted hypervelocity impact experiments in order to explain the implantation of an impactor onto Vestan regolith, and also the surface of Ceres. They fired basalt and aluminium spherical projectiles, approximately 6.35 mm in diameter, onto pumice and highly porous ice targets at speeds between 4.5 and 5.0 km s^{-1}. Surviving projectile fragments ranged from approximately < 105 µm to 5 mm. Based on their results, it was inferred that both Vesta and Ceres should have significant levels of exogenic material delivered via impacts.

In parallel to this, renewed interest in the distribution of organic (and possibly even biological material) around the Solar System as contents of small rocky bodies etc., has led to a steady increase in the number of laboratory studies into the survival of projectiles. For example, the survival of biomarkers in projectile fragments in hypervelocity experiments has been studied (e.g., see Bowden et al., 2008; Parnell et al., 2010; Burchell et al., 2014a). Furthermore, even the survival of diatom fossils in projectile fragments has been demonstrated in laboratory experiments (Burchell et al., 2014b, 2017). This indicates that not only can projectile fragments survive after impact, they can deliver a wide variety of materials to the target bodies.

The subsurface regions at man-made impact sites should also contain impactor material. For example, consider the crater on comet 9P/Tempel-1 arising from the Deep Impact Mission (Schultz et al., 2013). This mission consisted of a 363 kg impactor (of which 49% was porous copper) impacting the comet nucleus at 10.3 km s^{-1} (A' Hearn et al., 2005; Veverka et al., 2013). In laboratory impacts onto ice targets at speeds up to 6.3 km s^{-1}, it has been shown that fragments of copper projectiles can survive at the impact site (McDermott et al., 2016). Extrapolating to the Deep Impact case, McDermott et al. (2016) predict the survival of between 8% and 15% of the copper projectile at the impact site. In that study, McDermott et al. (2016) also reported extensively on the progressive stages of disruption undergone by copper projectiles for impacts involving shock pressures up to 50 GPa, including providing size distributions of the fragments. Using high porosity targets, Avdellidou et al. (2017), have shown that whilst, in general, projectile fragment survival increases with increasing target porosity, this is not the case when target mineral grain size exceeds projectile size.

Given the growing interest in emplacement of projectile material onto targets after impact we have conducted a series of impacts in the laboratory, recovering the projectile material after impact. Here we look at the fragmentation of basalt and shale projectiles in normal incidence impacts at speeds from 0.39 to 6.13 km s^{-1}. The targets were water, a homogeneous target which is easily modelled and from which the projectile fragments can be readily recovered. We find Q_p^* and fragment size distributions, and compare to previous work. We also determine the possible sizes

for an impactor on Vesta using the cumulative fragment size distribution.

2. Method

2.1. Projectiles

The projectile materials used in this study were basalt and shale, mostly in the form of cubes, 1.5 mm along each edge, although in some shots basalt spheres (1.5 mm diameter) were also used. Basalt was used as a projectile type as it is often used as an analogue for chondrite meteorites (e.g. Daly and Schultz, 2016). Shale was chosen as a comparison material which has been used in previous impact studies (e.g. Parnell et al., 2010). The basalt cubes were cut from blocks collected from the Isle of Skye, Scotland, and were fine grained with small vesicles (mm sized). The composition of the basalt, as measured by SEM-EDX was: Olivine ($Fa_{80}Fo_{20}$), Clinopyroxene ($En_{10}Fs_{46}Wo_{43}$) and Feldspar ($An_{57}Ab_{32}Or_{11}$). The shale was also collected from Scotland. In both cases, the projectiles were cut by hand, and measured and weighed before use. The basalt glass spheres used were acquired from 'Whitehouse Scientific' (http://www.whitehousescientific.com/) and have a typical composition of SiO_2 (43%), Al_2O_3 (14%), CaO (13%), Fe_2O_3 (14%), MgO (8.5%), Na_2O/K_2O (3.5%) and others (4%). These spheres are the same as those used in Avdellidou et al. (2016).

2.2. The light-gas gun and the shot procedure

The projectiles were shot using the University of Kent's two stage light-gas gun (Burchell et al., 1999). The speed was selected in each shot by varying the pre-pressure of the light gas used in the gun's first stage. To achieve speeds below 1 km s^{-1}, the bursting disk, which separated the two stages in the gun, was calibrated to burst at specific pressures to ensure slow projectile speeds. The speed of the projectile was measured in-flight by passage through two laser screens with a known spatial separation, providing a speed determination to better than ± 1% (Burchell et al., 1999). When the gun was fired, the target chamber was evacuated to 50 mbar to avoid deceleration of the projectile in flight. The shot regime used here was from 0.51 to 6.02 km s^{-1} for basalt, and 0.39 to 6.13 km s^{-1} for shale (see Table 1).

The target in each shot was a thin plastic bag of water held in a metal frame, see Fig. 1a. The plastic was water rich and had a thickness of less than 50 µm, and in effect, acts as the surface layer of the water target in terms of the projectile impacts. There was approximately 250 ml of water in the target in each shot, and in the line-of-flight of the projectile there was a water column depth of typically 3 cm. Previous experiments with this target have shown that this is sufficient to contain the impact event without causing cratering in the rear surface of the target holder (Baldwin et al., 2007). During a shot the target holder stood in a metal tray with a metal cover over it (Fig. 1b). This design was to ensure maximum collection of the water after impact (a small aperture in the cover permitted entrance of the projectile).

After a successful shot the target was removed from the chamber and the water collected. The collected water, containing the fragmented projectile, was then filtered through a 0.1 µm Durapore membrane filter using a vacuum pump.

2.3. Fragment measuring

After each shot, the resulting Durapore filter paper was mapped in the University of Kent's Hitachi 3400-H Scanning Electron Microscope (SEM). The SEM was run at 20 kV, with a magnification of x95 and in variable pressure mode (90–110 Pa) to avoid charging as the samples were uncoated. The resulting map typically included at least 800 individual fields of view. Each image was then analysed using ImageJ software. ImageJ is a public domain, Java based script, designed to help computer analysis of images, and was developed at the NIH (https://imagej.nih.gov/ij/index.html, site accessed July 2017). This software draws an ellipse over the silhouette of each fragment (see examples in Fig. 2) and produces the area and semi-major (a) and semi-minor (b) axis of each individual ellipse (fragment). This procedure was used by Durda et al. (2015) for example, to accurately measure the *a* and *b* values of the 36 largest fragments from catastrophic disruption events of irregular and regular targets. Fragment volumes are obtained assuming an ellipsoid shape with semi-major axis, *a*, and semi-minor axes *b*. Here we isolate and identify fragments down to around 10 µm in size, and can find over 100,000 fragments in the higher speed shots. To account for contamination from material which was not the projectile, i.e. any fine bursting disk or sabot material which may accompany the projectile in a shot, a control shot was conducted. This control involved firing the gun in the same way as usual, but into ice (instead of water) and without a projectile in the sabot. Ice was used because any small gun debris would not be able to pierce the bag, meaning it could not be collected. The melted ice was analysed as usual and the size distribution of the resulting fragments measured. An insignificant amount of material above 10 µm was measured. A small correction was then made to the size distribution in each true shot, but as the data presented here are typically for fragment sizes over 10 µm there is little ef-

Fig. 1. (a) The ocean target frame in its base tray. The bag which contains the water is held between the two vertical plates whose separation can be adjusted. The impact direction is shown with the red arrow. (b) The cover which fits over the frame in (a). The projectile enters the cover in the hole seen in the face. The ruler is 30 cm long. (For interpretation of the references to colour in this figure legend, the reader is referred to the web version of this article.)

Table 1
Shot and projectile summary. The peak shock pressures were determined using the planar impact approximation (PIA, Melosh, 2013). To calculate pressure in the PIA, a linear wave speed relation of the form $U = c + Su$ is used, where u and U are the particle speed and shock speed (both in km s^{-1}), with separate values for C and S for projectile and target materials. For basalt and water values of C = 2.60 km s^{-1}, S = 1.62 and a density of 2860 kg m^{-3}, and C = 2.39 km s^{-1}, S = 1.33 and 997.9 km m^{-3} were used, respectively, (Melosh, 2013). For shale we used C = 2.30 km s^{-1}, S = 1.61 and a density of 2545 kg m^{-3} (Ahrens and Johnson, 1995). Any blank entries for the mean fragment diameter are due to the projectile not fragmenting; in such cases the original projectile was recovered with minor damage. For the inclined angle shots the fragment distribution was not measured hence there are no values given for mean fragment diameter. The control shot had no projectile therefore has no mass and peak shock pressure. The error on the mean fragment diameter is the FWHM.

Shot ID	Projectile material	Mass [mg]	Speed [km s^{-1}]	Peak shock pressure (PIA) [GPa]	Mean fragment diameter [μm]	$m_{L,p}/M_p$
S290715#1	Basalt	7.291	0.51	1.09	–	0.996
S100615#1	Basalt	8.141	0.64	1.41	–	0.996
S240615#1	Basalt	8.708	0.70	1.57	23.8 ± 21.9	0.177
S050815#1	Basalt	7.270	0.84	1.95	18.5 ± 14.0	0.003
S050315#1	Basalt	11.021	0.96	2.30	18.0 ± 10.9	0.009
G261115#1	Basalt	8.806	1.95	5.80	16.8 ± 8.2	0.003
G010515#2	Basalt	8.003	3.04	10.9	15.3 ± 6.5	0.004
G141015#1	Basalt	7.008	4.05	16.9	15.6 ± 7.0	0.001
G101215#1	Basalt	7.684	4.71	21.4	14.0 ± 5.3	0.002
G041115#1	Basalt	7.889	4.92	23.0	15.4 ± 6.6	0.001
G271114#1	Basalt	7.809	5.31	26.0	14.2 ± 5.7	0.001
G211015#2	Basalt	7.753	6.02	31.9	14.6 ± 5.8	0.002
G110516#1	Basalt[a]	5.143	1.98	5.93	18.0 ± 10.7	0.011
S270416#1	Basalt[b]	7.253	0.59	0.29	–	0.998
S110316#1	Basalt[b]	7.494	0.98	0.50	–	0.234
G200416#3	Basalt[b]	7.424	2.01	1.12	–	0.032
S280116#1	Shale	7.518	0.39	0.74	–	0.998
S030216#1	Shale	7.106	0.59	1.20	29.5 ± 36.8	0.291
S181115#1	Shale	7.136	0.95	2.12	22.7 ± 27.5	0.413
G130116#2	Shale	7.403	1.93	5.34	15.5 ± 7.7	0.038
G041115#1	Shale	6.465	3.12	10.3	15.5 ± 7.2	0.013
G031215#2	Shale	7.487	4.64	19.7	15.5 ± 6.6	0.006
G211015#2	Shale	8.083	6.13	30.9	16.0 ± 7.6	0.002
G250315#1	Control	–	5.36	–	14.6 ± 6.4	–

[a] Glass basalt sphere.
[b] Basalt cube shot at 15° angle of impact.

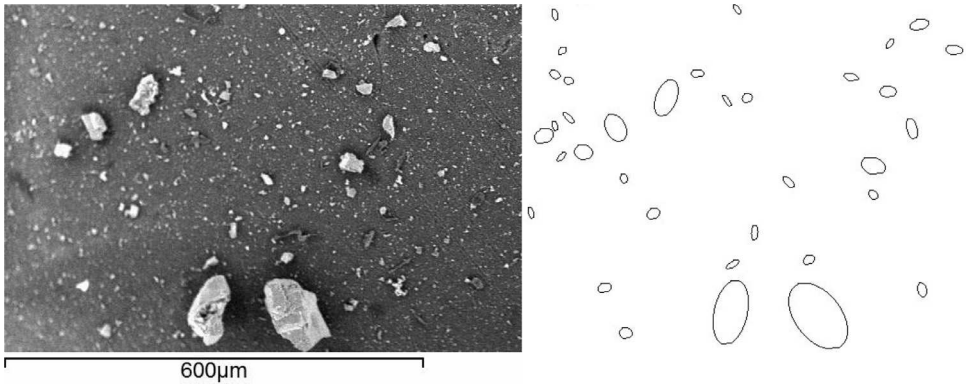

Fig. 2. SEM field of view for fragments at 0.70 km s^{-1} (left) and the ellipses fitted by the Image J software (right).

fect on the results. As a check on the ImageJ process, one sample was measured directly by eye on the SEM to confirm the accuracy of the software method. Good correspondence was found in both total number and size distribution.

2.4. Estimating the shock pressure

The Planar Impact Approximation (PIA) was used to determine the peak shock pressure upon impact. This provides an estimation of maximum pressures computed from the Hugoniot equations and the equations of state (Melosh, 2013). The PIA is valid so long as the lateral dimensions of the projectile are small compared with the distance the shock has propagated. It requires a linear shock wave speed relation in the form $U = C + Su$, where U is the shock speed and u is the particle speed (both in km s^{-1}). Separate values are required for C and S for both the projectile and target materials. From Melosh (2013) we take the values for basalt of $C = 2.60$ km s^{-1}, $S = 1.62$ and a density of 2860 kg m^{-3}, and $C = 2.39$ km s^{-1}, $S = 1.33$ and density of 997.9 kg m^{-3} for water. For shale we used $C = 2.30$ km s^{-1}, $S = 1.61$ and a density of 2545 kg m^{-3} (Ahrens and Johnson, 1995). Values for the peak shock pressure estimated using the PIA, for each shot are given in Table 2.

To compare to the peak shock pressure from the PIA we also used the ANSYS Autodyn 3D hydrocode to model the impacts (see Hayhurst and Clegg, 1997). This used both the projectile and target material equation of state (EOS) and a Von Mises strength model for the projectile. We used a shock EOS with the same values as that used in the PIA. The values used for the strength model for basalt were a shear modulus of 8.0 GPa (Christensen et al., 1980) and yield stress of 200 MPa (Rocchi et al., 2002). For shale we used a shear modulus of 1.6 GPa (Fox et al., 2013) and yield stress of 62 MPa (Koncagül and Santi, 1998). The shape of the projectile (cubic or spherical) was allowed for in the appropriate simula-

Table 2
Comparison of peak shock pressures determined from the planar impact approximation (PIA) (see Table 1) and the results from runs of Autodyn as described in the main text. For the Autodyn results, we give three results per simulation. The 'Highest' and 'Lowest' are the largest and smallest values for the pressure in the projectile. The highest value was typically close to the impact point, and the lowest is to the rear trailing portion of the projectile. The 'median' value is that to which 50% of the projectile was subject.

Speed [km s^{-1}]	Material	PIA [GPa]	AUTODYN-3D [GPa]		
			Highest	Median	Lowest
0.51	Basalt	1.09	2.14	0.44	0.05
0.64	Basalt	1.41	2.71	0.60	0.05
0.70	Basalt	1.57	3.00	0.68	0.06
0.84	Basalt	1.95	3.63	0.85	0.07
0.96	Basalt	2.30	4.20	1.05	0.07
1.95	Basalt	5.80	8.96	3.07	0.23
3.04	Basalt	10.9	14.6	6.07	0.84
4.05	Basalt	16.9	20.2	9.79	1.34
4.71	Basalt	21.4	24.0	12.1	1.79
4.92	Basalt	23.0	31.0	12.6	1.66
5.31	Basalt	26.0	30.5	13.9	2.07
6.02	Basalt	31.9	48.3	21.5	3.50
0.39	Shale	0.74	1.18	0.28	0.01
0.59	Shale	1.20	1.87	0.47	0.02
0.95	Shale	2.12	3.07	0.93	0.06
1.93	Shale	5.34	6.66	2.78	0.36
3.12	Shale	10.3	11.4	5.72	0.91
4.64	Shale	19.7	33.2	9.88	1.73
6.13	Shale	30.9	53.3	20.6	4.95

tion. This allowed us to see the distribution of peak shock pressure throughout the bulk of the projectile and not just near the contact phase as in the case of the PIA. In particular, corners can be an issue for non-spherical impactors, so by using 3D simulations we try to take this explicitly into account. Peak pressures across the projectile calculated using Autodyn, are given in Table 2.

3. Results and discussion

There were a total of 24 shots in this work (16 with basalt, 7 with shale and 1 control). Table 1 summarises each shot and gives the mass of each projectile, the peak shock pressure, the mean fragment diameter and the ratio of the largest fragment mass to the projectile mass ($m_{L,p}/M_p$). Table 2 gives the shock pressures determined by the PIA and the Autodyn hydrocode simulation for each shot. In Autodyn, the peak shock pressures were determined at 250 points evenly spaced over the whole volume of the projectile. This allowed for the peak pressure not being a single value across the body, and permits reasonable identification of the both the maximum and minimum pressures in the projectile. In addition, we also give in Table 2 the median peak shock pressure in the samples, which provides a more complete picture of the shock pressure inside the projectile. From Table 2, it can be seen that the peak shock pressure calculated using the PIA lies between the maximum and median values found by Autodyn, and is typically some 50% of the maximum value at low speeds (0.5 km s^{-1}), rising to 75% at intermediate speeds (4 km s^{-1}), and finally back to 60% at 6 km s^{-1}. It is therefore a reasonable indicator of the peak shock in a finite volume of the sample (and not just at a single point), so we use it as the measure of shock pressure in the subsequent analysis. However, it should always be recalled that there are more lightly shocked regions in each impactor and that when cubes are used there can be particular effects in corner regions.

Fig. 3 shows how the pressure measured by at two points (#234 at the front and #9 at the back of the projectile) in the Autodyn simulation changed with time for the 6.02 km s^{-1} basalt impact. Position 234 was a computational cell in the leading half of the projectile and which was numerically eroded in the simulation,

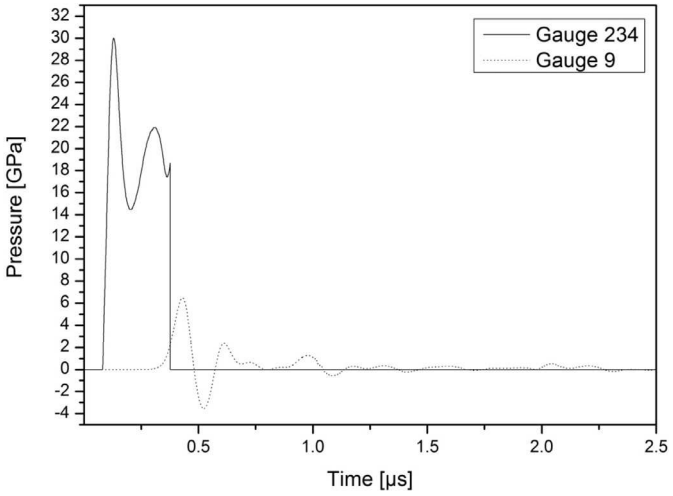

Fig. 3. Pressure readings for two positions in the Autodyn simulation, at the front (#234) and back face (#9) of a 1.5 mm cube shaped basalt projectile impacting water at 6.02 km s^{-1}.

hence the sudden fall to zero GPa. Position 9 was positioned in the latter half of the projectile and therefore the shock wave reached it later. After the initial compression (increase in pressure) there was an expansion of the material (represented by a negative pressure). This pattern of behaviour repeated for approximately 6 μs. The difference in peak shock pressure between the two points shows that material at the rear of the projectile received a considerably lesser shock than that at the front. Note that these positions did not record the highest or lowest peak shock pressures in the event. The positions which recorded the highest pressure (peak shock pressure) were positioned just behind the front impacting face, and the lowest were at the rear of the projectile.

3.1. Morphology of projectile fragments

Fig. 4 shows example SEM fields-of-view for three typical basalt shots (0.96, 3.04 and 5.31 km s^{-1}). These show the average size of the fragments are getting smaller with increasing impact speed (sizes are given in Table 1).

Fig. 5 shows the ratio of the semi-minor (b) to semi-major (a) for all fragments measured in typical shots, where a ratio of 1 refers to a circle and 0.1 to a bar shape. At the lower speeds, both basalt and shale had a high mean value of b/a. However, for basalt this rapidly reduced to $b/a \sim 0.55$ by speeds of 1 km s^{-1} and is then stable. For shale, the value of b/a of ~ 0.55 is only reached for impact speeds of approximately 4.5 km s^{-1} and above. This suggests that initially when the projectile has been disrupted, the fragments appear to be more spherical on average, but with increasing impact speed/pressure they are more elliptical, and that this is material dependent.

In Fig. 6 we show the mean value of each b/a plot and how it changes with impact speed (also see Table 3). When excluding the partially disrupted shots (shots < 1 km s^{-1}), the averages are 0.58 ± 0.16 (basalt) and 0.59 ± 0.14 (shale) as represented in Fig. 6. Therefore both basalt and shale projectiles appear to have similar morphologies upon disruption, but shale requires a higher speed and a greater shock pressure to achieve this level of disruption.

3.2. Cumulative fragment size distributions (CFSD)

In Fig. 7, we present some typical cumulative fragment size distributions (normalised to the original projectile diameter) for six typical shots (3 basalt and 3 shale) at a range of speeds. Each cumulative fragment size distribution has been fitted with power

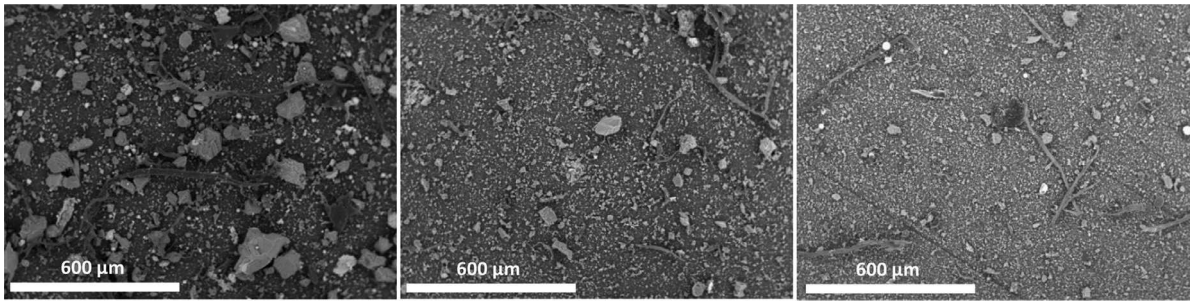

Fig. 4. Example SEM field of views of basalt fragments for impact speeds of 0.96, 3.04 and 5.31 km s^{-1}. Images are from backscattered electrons, in variable pressure mode (100 Pa), with accelerating voltage 20 kV. Some long thin fibres are present in the images and these are excluded from the analysis as they are not mineral in nature.

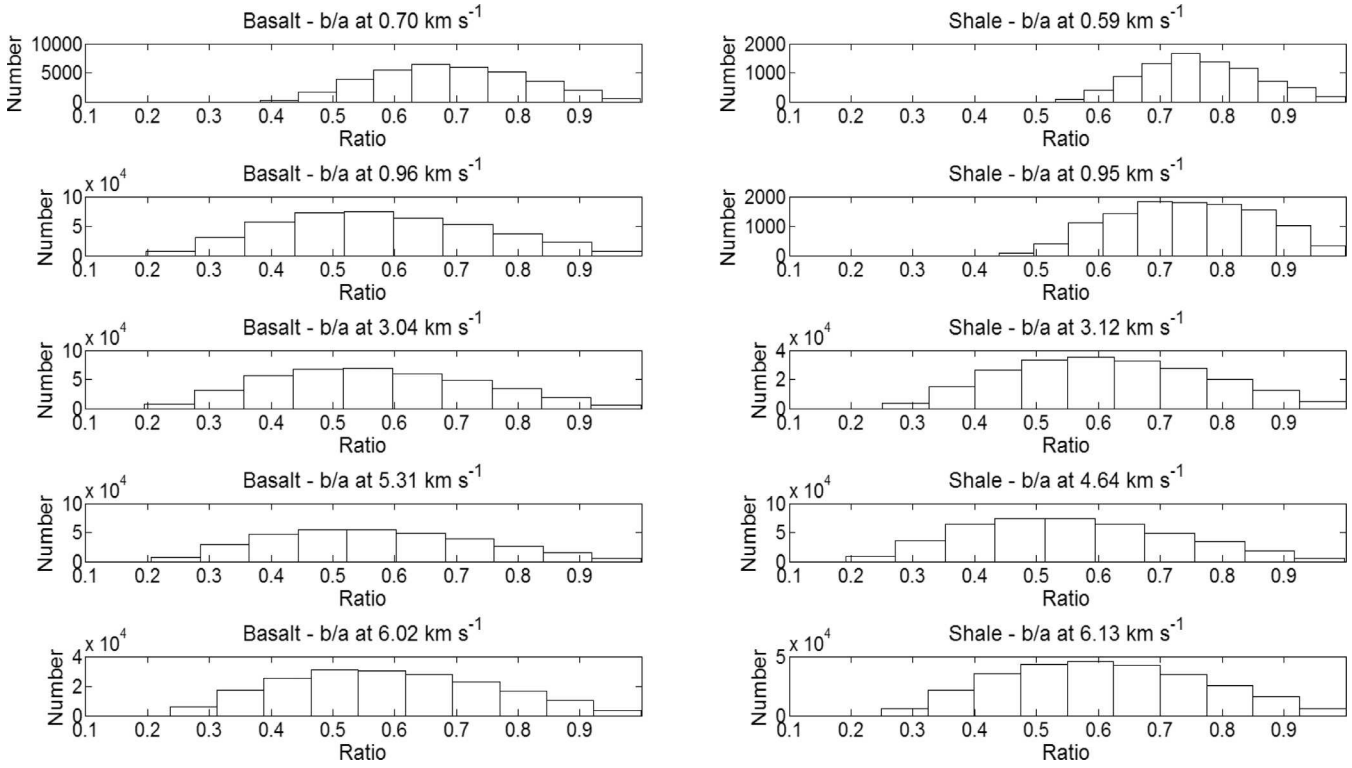

Fig. 5. Histogram of the ratio of the semi-minor (b) to semi-major (a) for all fragments measured in these shots. A ratio of 1 implies a circle shape, and 0.1 a bar-like shape.

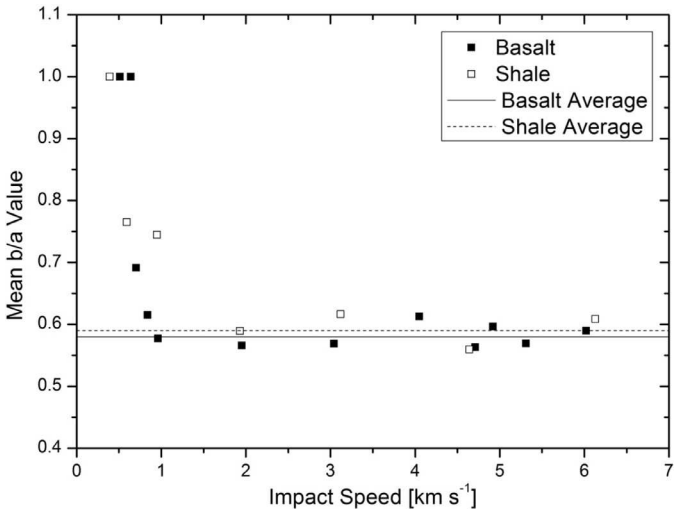

Fig. 6. Mean b/a values for each shot. The two lines refer to the mean values for basalt (solid line) and shale (dotted line), excluding the slower speed shot data.

laws in the form $N(>S) = aS^b$, where N is the number of fragments greater than a given size S. A single power b did not fit the entire size range for any shot, so we have divided each size range into three. These refer to the large sized fragments, intermediate sized fragments and small sized fragments in each shot. The approximate normalised size ranges are < 0.05, 0.05–0.1 and > 0.1 for small, intermediate and large respectively. The power b values for basalt and shale are given in Table 4.

In Fig. 8 we show how the power b changes with increasing impact speed. It would appear that for slower shots (partial fragmentation domain) the gradient of the large fragments is shallower than the intermediate or small size ranges. This is because the large projectile fragments in these shots have not been broken up into multiple smaller similarly sized fragments. As speed increases above 1 km s^{-1} for basalt, there is a sudden large change in the slope for the large fragments from approximately -2 to approximately -5 or -6. This jump does not occur for shale until the speed exceeds approximately 3 km s^{-1}. This parallels the change in b/a ratios in the two materials vs. speed.

Overall, each size section appears to get steeper (larger b) with increasing impact speed. This is most evident in the larger frag-

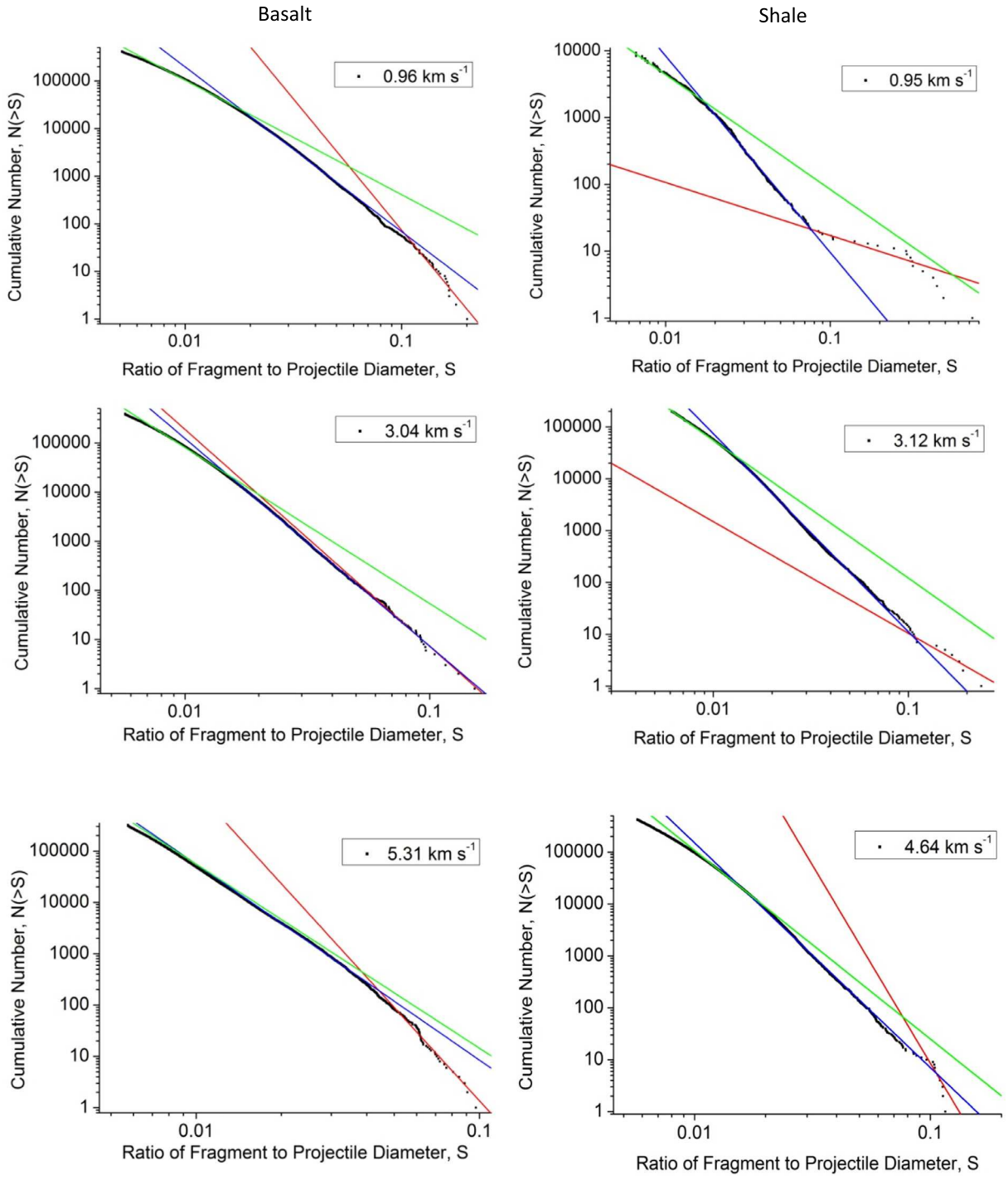

Fig. 7. Cumulative fragment size distributions (normalised to the original projectile diameter) for six typical shots. The left plots are basalt and the right shale. The lines are fits in each size region (green for small sizes, blue for intermediate, and red at largest sizes). The slope of each fit line is given in Table 4. (For interpretation of the references to colour in this figure legend, the reader is referred to the web version of this article.)

ments. This is explained by the increasing shock pressure breaking larger fragments into multiple similar sized fragments. Hence, at the highest impact speed (greatest shock pressure) there are fewer larger fragments.

3.3. Survival/retained projectile percentage

Assuming that each fragment's mass is approximately equal to the mass of an ellipsoid calculated, as stated above, using the semi-major (a, x_i) and minor (b, y_i) axis, and knowing the density (ρ) of the material, we can deduce an approximation of the mass of each fragment. From this we can determine a percentage of projectile survival based on the recovered fragments:

$$Total\ Survived\ Mass = \sum_{i=0}^{N} \frac{4}{3}\rho\pi x_i y_i^2. \quad (1)$$

This assumes the third axis, not seen in the 2D SEM images, is equal in size to the smaller of the two measured axes.

In Fig. 9 the estimated surviving mass percentage against the peak shock pressure in each shot is shown. For basalt there is a

Table 3
Summary of the mean ratio of the semi-major and semi-minor axes (b/a) values for basalt and shale cubes fired at each speed. The standard error on the mean is given in each case, along with σ, the standard deviation of the distribution about the mean.

Impact speed [km s^{-1}]	Mean b/a	Standard error ($\times 10^{-4}$)	σ
Basalt			
0.51	1.00	–	–
0.64	1.00	–	–
0.70	0.69	6.45	0.12
0.84	0.62	5.33	0.16
0.96	0.58	2.53	0.16
1.95	0.57	2.86	0.16
3.04	0.57	2.60	0.16
4.05	0.61	4.03	0.16
4.71	0.56	2.83	0.16
4.92	0.60	3.86	0.17
5.31	0.57	2.88	0.16
6.02	0.59	3.75	0.16
Shale			
0.39	1.00	–	–
0.59	0.77	10.0	0.09
0.95	0.74	11.0	0.11
1.93	0.59	3.28	0.16
3.12	0.62	3.42	0.16
4.64	0.56	2.50	0.16
6.13	0.61	3.02	0.16

good power law fit:

$$Surviving\ \% = 115P^{-0.49}, \quad (2)$$

where P is the peak shock pressure in GPa. The goodness of fit for this is $r^2 = 0.9449$.

The same power law fit for the shale data gives:

$$Surviving\ \% = 100P^{-0.33}. \quad (3)$$

The goodness of fit for the power law fit to shale is $r^2 = 0.8444$.

Shale appears to have a higher surviving mass percentage at the higher shock pressure. We considered if this was an artefact of Eq. (1), whereby the third axis of each fragment (the depth) is not measured and is assumed to be equal to the semi-minor axis. However, upon further investigation of the fields-of-view the fragments of shale do not appear to be particularly flat (or 'plate' shaped) compared to the basalt. Looking at Fig. 7, at a given impact speed the largest fragment of shale is larger than the largest fragment in the basalt shots. Given that most mass resides in the larger fragments, this may explain why shale gives more complete mass recovery than basalt in these impacts. Mass can be lost via two routes. The first is due to the mass present in fragments of a size below the experimental resolution. A second mechanism is removal of projectile fragments from the impact site mixed with target material ejecta during the impact process. The mixing of projectile material with target ejecta has been shown experimentally by, for example, Burchell et al. (2012).

4. Discussion

4.1. Large fragments

In Fig. 10 we display the behaviour of fragment size distributions at the very largest sizes, which depend sharply on impact speed. At slower speeds the fragment size distributions have a concave shape. At intermediate speeds (approximately 3 km s^{-1}) this flattens out. Finally, at higher speeds there is a convex shape. This behaviour is seen in the largest fragments of disrupted targets (Durda et al., 2007; Leliwa-Kopystynski et al., 2009) and is related to the object transitioning from a partially disrupted to a heavily catastrophically disrupted regime. As the energy density increases, the larger fragments (which appear in the slower speed impacts) are replaced by multiple smaller fragments. Thus the behaviour normally associated with disruption of targets, appears also to hold for fragmentation of projectiles.

4.2. Survival estimates for impacts on the Moon, Mars, Asteroids and Pluto

We use the fit (Eq. (2), Fig. 9) to deduce an estimation of the impactor survival percentage in different impact scenarios. In

Table 4
Summary of all fitting values for each power law and size section of the cumulative fragment size distributions (examples of which are shown in Fig. 7). The power law is in the form of $N(>S) = aS^b$, where N is the number of fragments greater than a given size ratio S. Where no entries are given the projectile was recovered virtually intact. Also given is the square of the regression coefficient for each fit (R^2).

Speed [km s^{-1}]	Small			Intermediate			Large		
	a ($\times 10^{-3}$)	b	R^2	a ($\times 10^{-3}$)	b	R^2	a ($\times 10^{-3}$)	b	R^2
Basalt cube									
0.51	–	–	–	–	–	–	–	–	–
0.64	–	–	–	–	–	–	–	–	–
0.70	139.6	−2.64	0.9986	12.1	−3.54	0.9911	497.7	−1.66	0.9495
0.84	62.8	−2.36	0.9964	31.4	−3.25	0.9960	582.4	−1.63	0.9880
0.96	1623.6	−2.40	0.9972	24.0	−3.46	0.9982	0.2	−5.51	0.9845
1.95	10.8	−3.49	0.9995	0.6	−4.24	0.9944	0.04	−5.17	0.9876
3.04	36.2	−3.17	0.9948	0.4	−4.22	0.9992	0.3	−4.41	0.9833
4.05	60.3	−2.91	0.9990	2.3	−3.68	0.9998	0.01	−5.28	0.9769
4.71	21.0	−3.13	0.9940	0.1	−4.70	0.9979	0.01	−5.02	0.9370
4.92	2.8	−3.62	0.9984	0.3	−4.18	0.9981	0.02	−5.06	0.9293
5.31	3.8	−3.58	0.9990	1.3	−3.81	0.9969	0.001	−6.05	0.9923
6.02	2.1	−3.69	0.9965	0.2	−4.19	0.9973	0.0001	−6.88	0.9891
Basalt sphere									
1.98	1900	−2.41	0.9791	16.7	−3.66	0.9966	0.14	−6.25	0.9351
Shale									
0.39	–	–	–	–	–	–	–	–	–
0.59	14,165.2	−1.19	0.9893	114.0	−2.42	0.9987	1595.1	−1.17	0.9466
0.95	1612.1	−1.72	0.9897	11.0	−2.94	0.9881	2772.8	−0.79	0.9216
1.93	52.3	−3.00	0.9992	1.6	−3.83	0.9998	150.5	−2.26	0.9927
3.12	269.2	−2.66	0.9973	1.7	−3.82	0.9990	73.5	−2.15	0.9317
4.64	5.9	−3.63	0.9992	0.3	−4.33	0.9961	0.0002	−7.63	0.8260
6.13	11.2	−3.40	0.9984	0.4	−4.35	0.9987	0.001	−6.53	0.9250

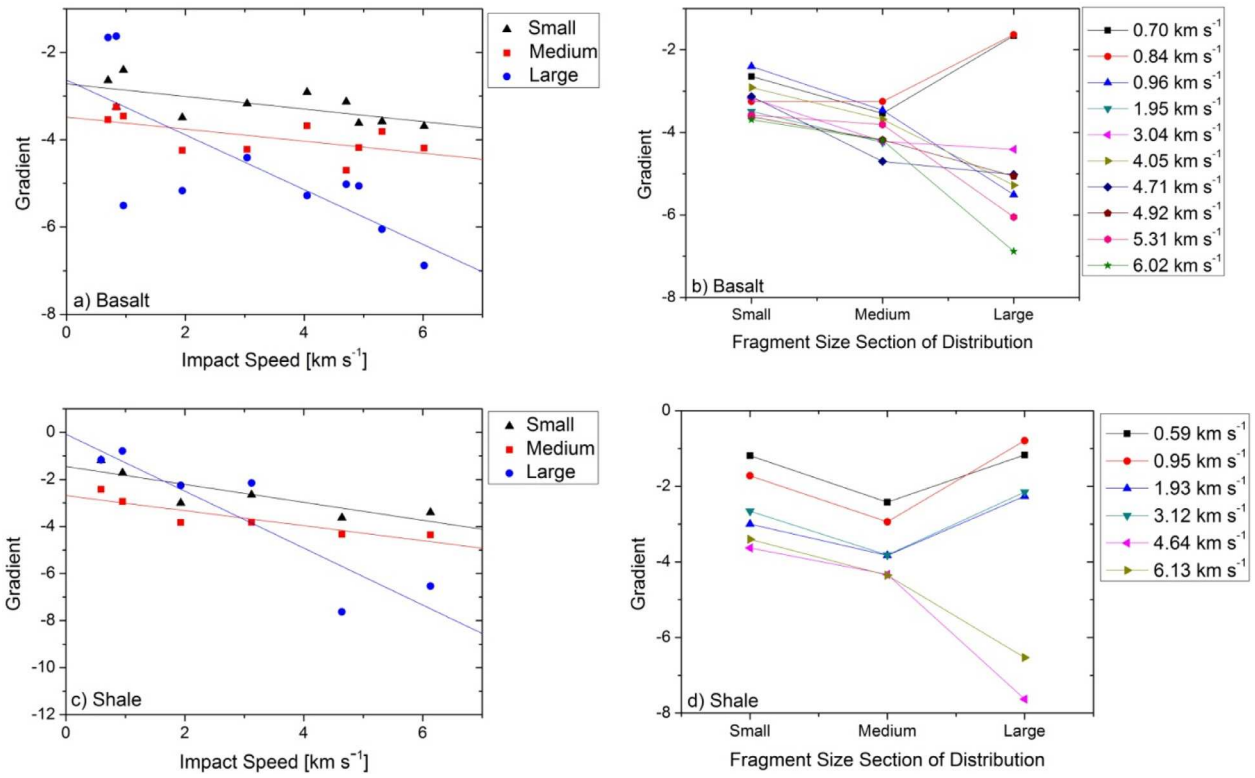

Fig. 8. The gradients of the cumulative fragment size distribution (see Fig. 7) vs (a) impact speed and (b) by size regime for basalt, and similarly (c) and (d) are for shale. The fit lines in (a) are gradient = $-0.144x^{-2.72}$, $-0.138x^{-3.48}$ and $-0.628x^{-2.63}$ for the small, medium and large fits respectively. In (c) the fits are gradient = $-0.381x^{-1.45}$, $-0.319x^{-2.69}$ and $-1.21x^{-0.08}$ for the small, medium and large fits, respectively.

Table 5
Estimate of the percentage of impactor survival in different solar system impact scenarios. The peak shock pressure was determined using the PIA and the percentage survival was obtained from the equation shown on Fig. 10.

Body	Speed [km s^{-1}]	Shock Pressure [GPa]	Percentage Survival	Reference for impact speed
Pluto	1.9	4.6	54	Zahnle et al. (2003)
The Moon	2.3	8.9	39	Burchell et al. (2014a)
Mean collision Speed in the Asteroid Belt	5.0	48	17	Bottke et al. (1994)
Mars	9.3	135	10	Steel (1998)

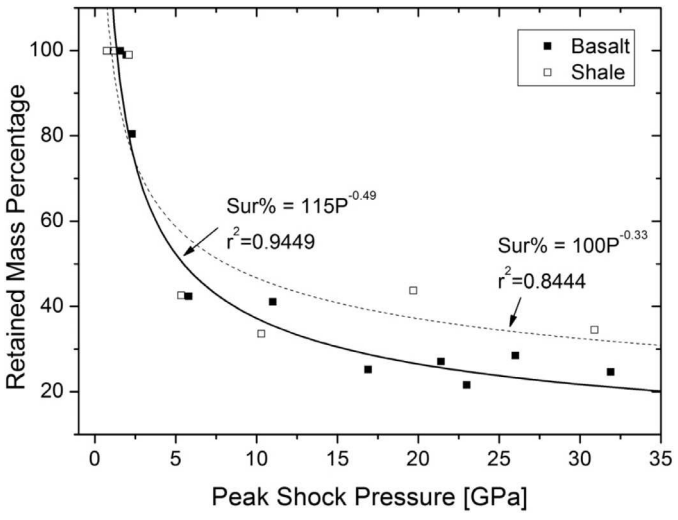

Fig. 9. Projectile surviving mass at peak shock pressures determined using the PIA. The solid line is a fit to the basalt data. The solid and dashed line is the fit for the basalt and shale data, respectively.

Table 5 we take the average impact speed on different solar system bodies, and, use the planar impact approximation to determine a peak shock pressure for that impact. The impactors are taken as basalt, and the target bodies are either regolith (sand), water ice or basalt (for the Moon, Pluto and both Mars and Asteroid belt, respectively). The appropriate C, S and density values for the target materials are 1.70 km s^{-1}, 1.31 and 1600 kg m^{-3} for regolith (dry sand), 1.32 km s^{-1}, 1.53 and 915 kg m^{-3} for water ice, and 2.60 km s^{-1}, 1.62 and 2860 kg m^{-3} for basalt (Melosh, 2013). Using the results for the PIA, combined with Eq. (2) we find an approximate surviving percentage of the projectile (see Table 5). When extrapolating to other bodies however, these surviving fractions should be considered upper limits. This is because other issues than fragmentation may influence retention at the impact site. For example, on small bodies, due to the low escape velocity more material may be lost as ejecta from a crater and not retained locally. As already pointed out (see above), ejecta can carry impactor material mixed with it.

These predicted values provide only a very rough guide owing to a lack of detailed knowledge relating to the effects of, for example, scaling to different projectile sizes, porosity in both projectile and target, differing local gravity influencing retention of ejecta, the influence of surface curvature on the impact events, etc.

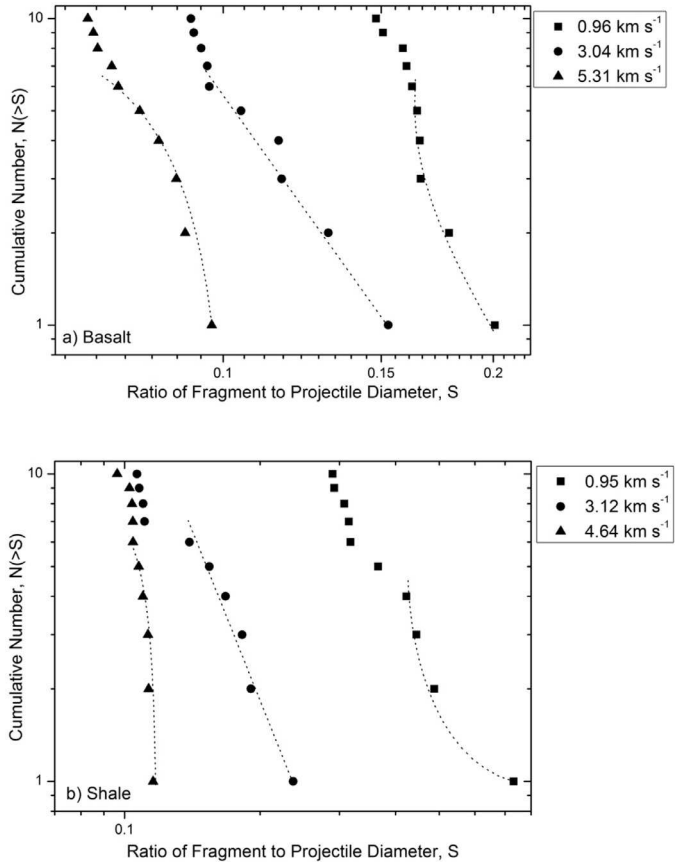

Fig. 10. Cumulative fragment size distribution (in log–log space) for the 10 largest fragments for (a) basalt and (b) shale at three typical impact speeds. At low speeds (right-most data set in each panel), the cumulative size distribution for the very largest fragments displays a concave behaviour (dotted line). At intermediate speeds this has flattened to a straight line and at the higher speeds (left-most data set in each panel) has become convex.

However they do suggest that Pluto and the Moon should have large amounts of impactor remnants on their surface (or in the sub-surface beneath impact craters). Furthermore, although it is a slight extrapolation from the data, it does suggest that 17% of material in an asteroid impact should survive. Additionally, the results in Table 5 suggest that of order 10% of the impactor could survive an impact on Mars. This is however a major extrapolation beyond the shock pressure regime in which the data were taken here. The curve in Fig. 9 does not vary greatly with shock pressure at high pressures, however, this result should be taken as approximate.

4.3. Onset of projectile disruption

The projectile energy density is determined by the equation below (Eq. (4)) (see Schultz and Gault, 1990a; Nagaoka et al., 2014).

$$Q_p(\theta) \equiv \frac{0.5 M_p v_i^2 \sin^2\theta}{M_p} = 0.5 v_i^2 \sin^2\theta, \tag{4}$$

where M_p is the mass of the projectile, v_i is the velocity of impact and Θ is the angle of impact from the target surface (where for normal incident impacts this gives $\sin^2\theta = 1$). It is assumed that energy lost in fragmentation greatly exceeds other internal energy losses such as deformation. The fragmentation limit, Q_p^*, is defined as the minimum specific energy required to disrupt the projectile so that the mass of the largest fragment equals 50% of the original projectiles' mass ($m_L/M_p = 0.5$).

In Fig. 11 the data for m_L/M_p vs. Q_p are shown for all impacts of the cube shaped projectiles at normal incidence. We fit one trend line to the shale data. By contrast the basalt appears to display two trend lines, as there are several distinct regions apparent in the data in this projectile energy density range.

The equations of the lines are; for shale ($r^2 = 0.9278$):

$$\frac{m_L}{m_p} = 1.05 \times 10^5 Q_p^{-1.07}, \tag{5}$$

and for basalt where $Q_p < 10^6$ J kg^{-1} ($r^2 = 0.9967$):

$$\frac{m_L}{m_p} = 4.58 \times 10^{22} Q_p^{-4.27}, \tag{6}$$

and where $Q_p > 10^6$ J kg^{-1} ($r^2 = 0.9852$):

$$\frac{m_L}{m_p} = 2.50\ Q_p^{-0.46}, \tag{7}$$

where Q_p is in J kg^{-1}. From Eqs. (5) and (6) we deduce the catastrophic disruption energy densities to be 9×10^4 J kg^{-1} and 24×10^4 J kg^{-1}, for shale and basalt respectively. This is a factor of ~2.5 difference between the two materials.

Schultz and Gault (1990a) suggest that the energy partitioned into the projectile fragmentation, ΔE_{PF}, can be split into the energy partitioned into fragmentation after impact, ΔE_F, and the energy wasted in getting to the fragmentation limit, ΔE_oEq. (8).

$$\left(\frac{\Delta E_{PF}}{m_p}\right) = \left(\frac{\Delta E_F}{m_p}\right) + \left(\frac{\Delta E_o}{m_p}\right). \tag{8}$$

It was suggested by Schultz and Gault (1990a) that Eq. (8) can be rewritten by introducing the largest fragment mass, $m_{L,p}$, and rearranging terms:

$$\left(\frac{m_L}{m_p}\right) = \left(\frac{m_L}{m_p}\right)_{CD}\left(\frac{\Delta E_F}{\Delta E_{PF}}\right) + \left(\frac{m_L}{m_p}\right)_{PD}\left(\frac{\Delta E_o}{\Delta E_{PF}}\right), \tag{9a}$$

$$= a\left(\frac{\Delta E_F}{\Delta E_{PF}}\right)_{CD} + b\left(\frac{\Delta E_o}{\Delta E_{PF}}\right)_{PD}, \tag{9b}$$

where a and b represent fractions of the original projectile mass that define partial and catastrophic disruption, respectively, (Schultz and Gault, 1990a). The first term can be shown to be equivalent to the projectile strength S (given by the tensile strength of the material), divided by the peak vertical stress σ_θ, or, equivalently, when catastrophic disruption dominates failure:

$$\frac{m_L}{m_p} \sim \left(\frac{\sigma_\theta}{S}\right)^{-1} \sim \left(\frac{\rho_p Q}{S}\right)^{-1} \sim \left[Q\left(\frac{c_t \rho_t}{c_p \rho_p}\right)\sin^2\theta\left(\frac{S}{\rho}\dot{\epsilon}^{1/4}\right)^{-1}\right]^{-1} = [Q_c(\theta)]^{-1} \tag{10}$$

where $\dot{\epsilon}$ is the strain rate, c refers to speed of sound and ρ refers to the density. When partial disruption occurs, the second term in Eq. (9b) dominates. It can be shown that:

$$\frac{m_L}{m_p} \sim \left[Q \sin^6\theta\left(\frac{S}{\rho}\dot{\epsilon}^{1/4}\right)\right]^{-1} = [Q_o(\theta)]^{-1}. \tag{11}$$

Combining these equations gives:

$$\frac{m_L}{m_p} = \left[\frac{a}{Q_c(\theta)} + \frac{b}{Q_o(\theta)}\right], \tag{12}$$

where Q_c is the energy density when catastrophic disruption dominates failure, Q_o is the energy density when partial disruption occurs and the values of a and b can be derived empirically. a and b are not derived for the data in this work. However, Schultz and Gault (1990a) do derive a and b for their data.

In Fig. 12 we show results for m_L/m_p vs. Q_p from four separate studies; Schultz and Gault (1990a), Nagaoka et al. (2014), Avdellidou et al. (2016) and the results for basalt projectiles in this paper.

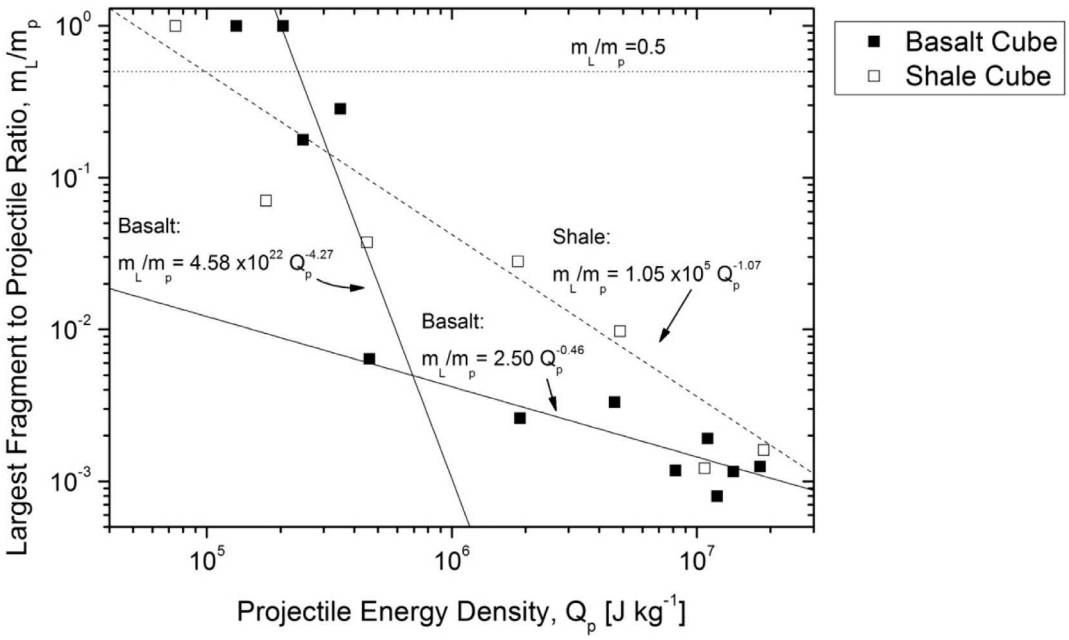

Fig. 11. Mass ratio of largest surviving fragment of projectile versus the projectile energy density, Q_p. The horizontal dotted line refers to the catastrophic disruption threshold, $m_L/m_p = 0.5$. The dashed and the solid lines are the fits to the shale and basalt, respectively. The fits were made in log–log space.

All these studies used basalt projectiles. Here we also include the data for the basalt sphere and non-normal incident impact from Table 1. As stated before, Schultz and Gault (1990a) fired basalt projectiles (diameter 5 mm) at inclination angles between 7.5° and 15° into sand and one shot into water; Nagaoka et al. (2014) fired basalt cylinders (5 mm in diameter and 5 mm in length) into sand; and Avdellidou et al. (2016) fired synthetic basalt spheres (diameter 2.0–2.4 mm) into ice.

The data in Fig. 12a follows two trends – Trend 1 (basalt impacts at normal incidence from this work) and Trend 2 (shots at non-normal incident, this work, and from Schultz and Gault (1990a) involving basalt onto sand at 7.5°). Trend 1 has almost intact projectiles recovered after the impact, until $Q \sim 10^5$ J kg^{-1}. The surviving fraction then falls off rapidly between 10^5 and 5×10^5 J kg^{-1} as disruption occurs. Above 5×10^5 J kg^{-1}, the projectile is fully disrupted and the gradient of the slope decreases.

The shots in Schultz and Gault (1990a) that were into sand were all fired at an angle of 7.5°. This means that the projectile energy density is considerably lower than that in this work, i.e. Q_p is lower due to the $sin^2\theta$ term in Eq. (4). Schultz and Gault (1990a) show that the projectile usually fragments at a much lower Q_p value than in our work at normal incidence; this is due to the shallow impact angle. The implication is that, although the non-normal incidence at a given impact speed should, according to Eq. (4), reduce the energy density in the projectile, it is actually leading to disruption at a significantly lower Q_p value. A plausible explanation, is that in shallow angle impacts, shear effects are important (i.e. so called "impact decapitation", Schultz and Gault, 1990b), unlike in more vertical impacts where it is the tensile strength that is critical.

In Fig. 12b we compare our work with that of Nagaoka et al. (2014). The data could (mostly) be taken as from a single data set with the same trend vs. Q_p, namely an initial step fall in m_L/m_p until $Q_p \sim 10^6$ J kg^{-1} (or $m_L/m_p \sim 0.01$), and then a shallower dependence on Q_p emerges. This suggests that there is no significant difference between impacts on sand (porosity 45%) and water. Target porosity is known to play a part in impact cratering process (see Love et al., 1993; Love and Ahrens, 1996), but it does not appear to have significantly influenced projectile disruption here.

Finally, in Fig. 12c we compare our results to those of Avdellidou et al. (2016) who used the same light gas gun facility as here, and similar sized projectiles of the same synthetic basalt, but fired onto solid ice target (porosity < 10%). Here the choice of target has clearly influenced the outcome of the event. Catastrophic disruption on ice occurs at an increased Q_p^* (by a factor of 10). We shot a basalt sphere into our water target at a similar speed to Avdellidou et al. (2016) to see if the shape of the projectile was significant (Avdellidou et al., 2016) used spheres rather than cubes as here). The result was closer to what we found from our other data with cube projectiles, rather than to that for the basalt spheres in Avdellidou et al. (2016). It therefore appears projectile shape is not a significant issue. It should be noted however that the spheres are a synthetic, glassy, basalt. So there is some structural difference between our cube shaped natural basalt projectiles and the synthetic spheres which may explain why the cube and spherical data in our work do not fully coincide – but this observation is based on one impact.

Next, we calculate the peak shock pressure at the catastrophic disruption threshold Q_p^*, for Nagaoka et al. (2014), Avdellidou et al. (2016) and this work. In Table 6 we take the Q_p^* values for basalt of 24×10^4 J kg^{-1}, 9.00×10^4 J kg^{-1} and 2.31×10^6 J kg^{-1} from this work, Nagaoka et al. (2014) and Avdellidou et al. (2016), respectively. From Eq. (4) we can deduce the associated impact velocities to be, 693 m s^{-1}, 424 m s^{-1} and 2149 m s^{-1}. Using the PIA, with the appropriate target values for C and S, and density taken from Melosh (2013), these impact speeds correspond to peak shock pressures of 1.55 GPa (our work), and 1.00 GPa (Nagaoka's work). Avdellidou et al. (2016) have estimated the peak shock pressure in their impacts using Autodyn as 1.32 GPa at 2.14 km s^{-1}. We thus find that disruption occurs at 1.55, 1.00 and 1.32 GPa, very similar values in all three experiments on a variety of target types. The yield strength of basalt rocks is very variable and sample specific. However, the yield strength of basalt (at low strain rate) is approximately 250 MPa (Schultz, 1993). Therefore the peak shock pressure at the catastrophic disruption threshold for these three works is approximately 4–5 times that of the compressive yield strength

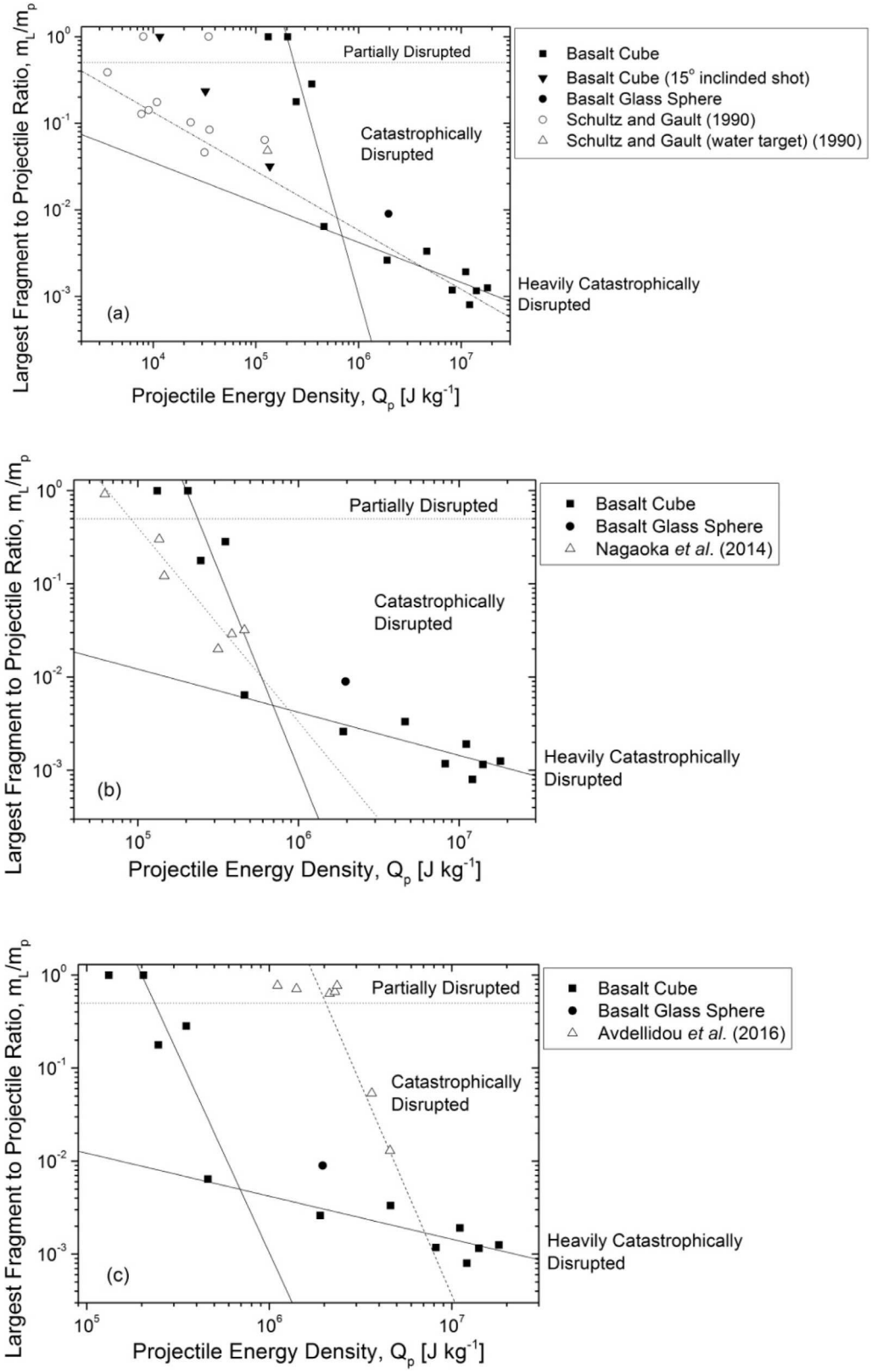

Fig. 12. Mass ratio of largest surviving fragment of projectile versus the projectile energy density, Q_p. For all the basalt impacts listed in Table 1, compared to data from (a) Schultz and Gault (1990a), (b) Nagaoka et al. (2014) and (c) Avdellidou et al. (2016). The horizontal dotted line refers to the catastrophic disruption threshold, $m_L/m_p = 0.5$. All other lines are fits to the data.

Table 6
Summary of the projectile energy density at catastrophic disruption and the corresponding impact speed for shale and basalt from this work, and basalt from Nagaoka et al. (2014) and Avdellidou et al. (2016).

Impactor	Q_p^* [J kg^{-1}]	Impact speed at the Q_p^* value [m s^{-1}]	Peak shock pressure (PIA) [GPa]	Reference
Shale	9.42×10^4	434	0.84	This work
Basalt	24×10^4	693	1.55	This work
Basalt	9.00×10^4	424	1.00	Nagaoka et al. (2014)
Basalt	2.31×10^6	2149	1.32	Avdellidou et al. (2016)

(at low strain rates) of basalt. For shale however, we find the peak shock pressure at Q_p^* was 0.84 GPa, which is some 14 times the yield strength.

4.4. Comparison to target fragmentation

The results here for projectile fragmentation (Table 6) can be compared to that for laboratory experiments concerning disruption of targets (see Ryan, 2000, for a review). For example, Takagi et al. (1984) disrupted targets of basalt at impact speeds from 70 to 990 m s^{-1}. (i.e. low speed impacts). They found Q^* for basalt of 473 J/kg, or 362 J/kg when they combine with other, similar data sets. These values are much less than those found here for projectile fragmentation. Holsapple et al. (2002) summarise a range of experimental laboratory results for target disruption, and for silicate targets again suggest a typical Q^* of a few hundred J kg^{-1}. However, these are cm scale targets, i.e. at a different scale to the projectiles used here.

Recently, Durda et al. (2015) reported on impact experiments on cm scale basalt targets at speeds of 4–6 km s^{-1}. All their experiments were above the catastrophic disruption limit, with the largest surviving mass fragment ranging from 0.24 to 0.02 times the original target mass. Taking the least disruptive of these as setting an upper limit, we obtain $Q^* < 2240$ J kg^{-1}. A power law fit to their data suggests $Q^* = 1321$ J kg^{-1}, but this is based on only 6 data points. This is greater than in the lower speed experiments, but still below what we find here for basalt projectiles. However, their target size is cm scale compared to mm scale for the projectiles here, and scale related strain effects change Q^* with size. For example Housen and Holsapple (1999) suggest that for granite, Q^* would increase by a factor of just over five for each decrease of an order of magnitude in size. This point is returned to below.

Durda et al. (2015) also reported on target fragment shape. They found a mean b/a ratio of 0.72 ± 0.13, greater than the value of 0.58 ± 0.16 we find here for basalt. They also reported on the cumulative mass distribution of target fragments, As usual, they find a power law behaviour, and give the power of −0.75 to −1.2 in the fragment mass range comparable to our intermediate size range. Since mass depends on size cubed, this is equivalent to a slope in size of −2.25 to −3.6, slightly smaller than what we find, which is −3.2 to −4.7.

Michikami et al. (2016), have also carried out impacts into (5–15 cm sized) basalt targets at speeds of 1.6–7.1 km s^{-1}. They agree with the earlier results of Fujiwara et al. (1978), that b/a is roughly constant around 0.7. Michikami et al. (2016) also report on cumulative mass distributions. They find a power law behaviour, where the power increases with Q (i.e. with increasing fragmentation). For low mass fragments they find the power ranges from −0.4 to −1.1. The lower values of −0.4 correspond to Q values of a few hundred J kg^{-1}. For the higher Q values their results are similar to Durda et al. (2015). Although they make no attempts to scale their results with size, Michikami et al. (2016) note that the shape ratios they find are similar to those of m sized boulders on asteroid 25143 Itokawa suggesting a catastrophic disruption origin for that body. This direct comparison of boulders (m scale) on Itokawa with the results of laboratory impact fragmentation experiments (cm scale) follows on from that of Nakamura et al. (2008) who also noted the similarities in shape. Michikami et al. (2018), revisit target fragmentation, looking at fragments sizes ranging from < 120 μm to > 4 mm. At small to medium sizes, they find b/a is constant at around 0.7 independent of the degree of fragmentation. They go on to note that b/a for Itokawa particles returned by the Hayabusa mission (see Tsuchiyama et al., 2014) have a mean of 0.67, and suggest that they are fragments from an impacted target. In Tsuchiyama et al. (2014), the cumulative size distribution of the Itokawa particles was found to be −2.0.

We can also compare to predictions from modelling. Benz and Asphaug (1999) model the disruption of basalt bodies at speeds of 3 km s^{-1}, and their results suggest that at the mm size scale here, Q^* should be approximately 2.3×10^4 J kg^{-1}. We note that at cm size scales, we have previously reported $Q^* = 1447 \pm 90$ J kg^{-1} for cement targets in our gun (Morris and Burchell, 2016), within a factor of 2–3 for similar targets reported elsewhere (Davies and Ryan, 1990; Fujiwara et al., 1989). More generally, Holsapple et al. (2002) summarise a range of predictions for Q^* vs target body size for rocky targets. Extrapolating the predictions in Holsapple et al. (2002), to the mm size scale here, suggests a range of values of Q^* from 5×10^3 – 5×10^4 J kg^{-1}. More recently, Leliwa-Kopystyński et al. (2016) use an analytic model for disruption of rocky bodies which produces similar results. So there is a range for Q^* for target bodies in the literature, but the value found here for the shale projectiles is twice the upper value in this range, and that for basalt is some 5 times larger than the upper value in the modelling.

4.5. Solar system implications

From the results here we can, assuming no size effects, scale to impacts on real bodies in the Solar System. Caution is needed however, strength is well known to be size dependent. For example, in catastrophic disruption of bodies, the energy density required to just disrupt a body, falls as body size increases. This is due to growth of cracks etc. being scale dependent, meaning that larger bodies are in effect weaker (see for example Holsapple et al., 2002). Similarly there are particular strain dependent effects that show up at small sizes. This is illustrated for example by Price et al. (2010, 2012, 2013) where the strength of several materials is shown to be highly non-linear above strain rates of 10^5 s^{-1}, rising by over an order of magnitude as strain rates increase to 10^8 s^{-1}. This regime is entered when projectile or target bodies are very small (less than say 10 μm). Whilst these small sizes are not relevant here, it does illustrate the difficulties of extrapolating from one size scale to another.

A full extrapolation of the results here to different size scales is thus difficult. No appropriate model is readily available which, at all size scales, produces for example size and shape distributions of fragments based on mineralogy of the impactors. We therefore follow the approach of Daly and Schultz (2015b, 2016), who attempt to identify key properties of laboratory scale experiments and compare to solar system scale examples. For example, if impactor fragments were identified, and the mean b/a ratio obtained for the fragments, a crude indication of impact speed can be ob-

Table 7
Fragment size and percentage survived information regarding impacts onto Vesta and Ceres. On Vesta the Veneneia and Rheasilvia craters are considered along with similar impacts on Ceres. The peak shock pressure for each impact was determined using the planar impact approximation (Melosh, 2013). By using the ratio of the diameter of projectile fragment to projectile from this work and the impactor size for Vesta or Ceres it is possible to determine the sizes of fragments. The percentage survival was determined using Eq. (2).

	Impact speed [km s^{-1}]	Impact angle	Size of impactor [km]	Peak shock pressure (PIA) [GPa]	Survival (%)	Size of largest fragment [km]	Size of typical mid size fragment [m]	Modal size fragment [m]
Vesta Scenarios								
Veneneia	2.00	45	50	8	43	8	1560	295
Veneneia	4.75	45	30	26	24	3	865	180
Rheasilvia	5.50	90	37	55	16	3	1000	230
Rheasilvia	5.50	45	90	32	21	8	2440	570
Ceres Scenarios								
Veneneia Conditions	2.00	45	50	6	48	7	1740	315
Veneneia Conditions	4.75	45	30	19	27	3	800	185
Rheasilvia Conditions	5.50	90	37	42	19	3	1000	235
Rheasilvia Conditions	5.50	45	90	24	24	12	2370	550

tained. That is to say, a high value of the mean b/a (0.6–0.7), would indicate a low speed (<1 km–s^{-1}) impact had occurred, whereas a lower mean value (~0.5–0.6) would suggest a higher speed impact. As already noted, it has been suggested by, amongst others, Durda et al. (2007) and Leliwa-Kopystynski et al. (2009), that when the largest fragments are observed in an asteroid family, the impact event can be labelled catastrophic or super-catastrophic etc. by the convex or concave nature of the shape of the large fragments in the CFSD. Applying the same logic to projectile fragment size distribution can indicate limits on the likely impact speeds.

The surface of the asteroid Vesta has dark material objects on the surface thought to be delivered via a carbonaceous chondrite impact (Reddy et al., 2012; Palomba et al., 2014; Daly and Schultz, 2016), as well as two large impact craters (Schenk et al., 2012). Reddy et al. (2012) states that the Veneneia crater, which is the second largest on the surface of Vesta, could have formed as the result of a 30 km diameter projectile impacting at 4.75 km s^{-1}, or a 50 km diameter projectile impacting at 2 km s^{-1}. The largest crater on Vesta, Rheasilvia, is postulated to have formed from either a 5.5 km s^{-1} impact of a 37 km impactor at 90°, or far larger diameter sized projectile impacting at the more probable angle of 45° (Ivanov and Melosh, 2013). Subsequently, Stickle et al. (2015) argued based on surface morphology, that the Rheasilvia impact feature was most likely the result of an impact at 5 km s^{-1} and $<40°$ incidence.

Using the data from this work it is possible to make some simple predictions regarding the fraction of impactor surviving an impact, the size of the largest fragment, size of a typical fragment and the size of the modal fragment (see Table 7). Firstly we determine the peak shock pressure using the PIA and assuming an impact on Vesta from a carbonaceous chondrite is effectively a basalt-on-basalt impact. The assumption that basalt can approximate carbonaceous chondrite is not strictly valid, the basalt being more competent and less porous. However, as noted by Daly and Schultz (2016), both materials will fail in a brittle way, and the resulting fragment size distribution will be influenced by the critical flaw size in each. For these reasons basalt is used here as an analogue for the carbonaceous chondrite material thought to impact Vesta. We then match the predicted pressure to the CFSD generation in this work at a similar peak pressure. Peak pressure is used rather than similar impact speed, as it is the shock pressures which are held to be critical for fragmentation. It is then possible to use Eq. (13) to determine fragment sizes on Vesta.

$$\frac{d_{FV}}{d_{iV}} = \frac{d_{FS}}{d_p}, \tag{13}$$

where d is object diameter and the subscripts FV mean fragment on Vesta, iV the impactor (on Vesta), FS meaning fragment in the relevant shot, and p the projectile in the shot. Note that we have ignored any scaling issues and assumed that the same ratios will apply at both scales. It should be noted that this analysis assumes the projectile fragments do not co-mingle with target material forming new composite particles.

One way to consider the scaling issue would be to consider the modelling of the variation of Q^* for target bodies in impacts (see Section 4.4 above). For example, Benz and Asphaug (1999), model the disruption of basalt bodies at speeds of 3 km s^{-1}. Their model includes a strain rate dependent strength term. They report that the mass of the largest fragment in their models depends only on a simple linear function of the impact energy density normalised to Q^* and not on target size; this remarkable result holds even though the simulations span bodies ranging from cm to 100 km scales. There is however, a slight dependence on impact speed. As an example, if the same speed behaviour holds here, then as we go from 3 to 5 km s^{-1}, at a given value of Q (50% larger than Q^*), we would find an increase in the largest fragment size according to Benz and Asphaug (1999) of about 10%.

Therefore, finding the ratio for the largest, typical and modal projectile fragments, and multiplying by the impactor size, it is possible to determine impactor fragment sizes on Vesta. The same is done with impacts on Ceres. However due to Ceres' lower density and higher porosity the peak shock pressure is modelled as basalt impacting permafrost ice. The appropriate values needed for permafrost in the PIA are density = 1960 kg m^{-3}, C = 2.51 km s^{-1} and $s = 1.29$ (Melosh, 2013). The peak shock pressure can then be used in Eq. (2) to determine the amount of the projectile surviving at the impact site post impact.

For Rheasilvia impact scenarios, in the cases of normal incidence impacts, the peak shock pressure exceed those in our experiments (max. of 31.9 GPa). We therefore use the CFSD from the impact at 31.9 GPa in the higher pressure scenarios, although this may introduce some inaccuracy.

For a 50 km projectile impacting at 2 km s^{-1} to form the Veneneia crater we predict the largest fragment size to be 7.6 km in diameter. A typical and modal size would be 1.6 km and 295 m, respectively. Furthermore, 43% of the impactor could survive. For the other possible impact event to form Veneneia (i.e., a 30 km dia. impactor at 4.75 km s^{-1}) we get modal, typical and largest fragment sizes of 185 m, 865 m and 2.9 km, respectively, and a survival percentage of 24%. For the same conditions for an impact on Ceres we find very similar fragment sizes (see Table 7).

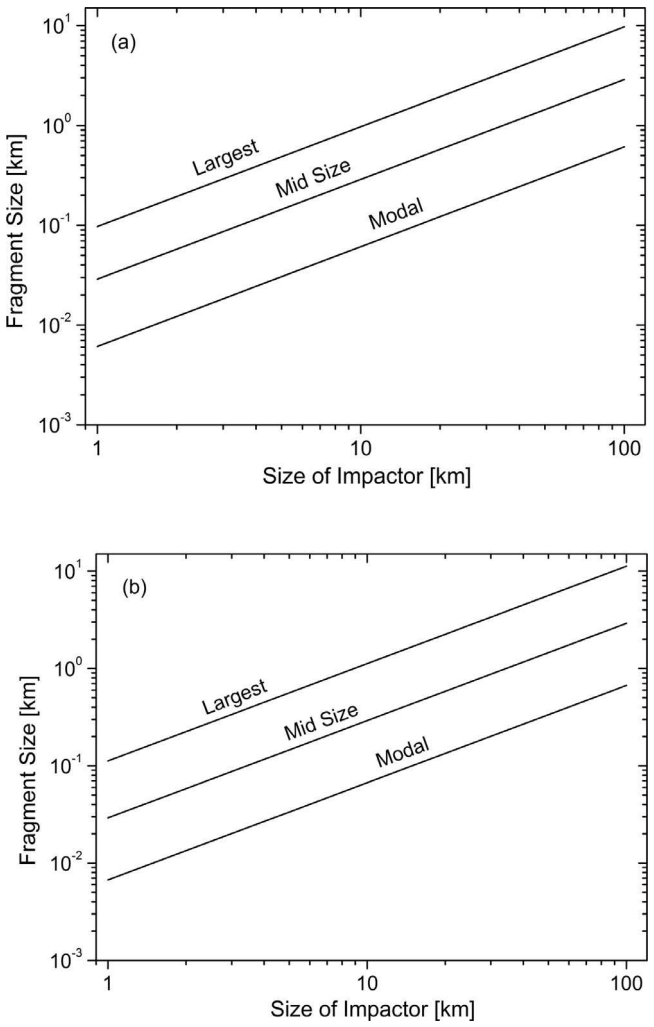

Fig. 13. Log–log plot of predicted fragment size vs. the size of impactor for (a) Vesta and (b) Ceres. For Vesta, each impact was modelled as a basalt projectile impacting a basalt target at 45° incidence at the average impact speed on Vesta of 4.75 km s^{-1} (Reddy et al., 2012). For Ceres, it was a basalt projectile onto a permafrost target at 45° at 5 km s^{-1} (the mean collision speed in the asteroid belt, Bottke et al., 1994). The peak shock pressures were determined using the planar impact approximation (Melosh, 2013).

It is also possible to consider the fragment sizes from a range of impactor sizes on Vesta and Ceres. We assumed 45° incidence and mean impact speeds of 4.75 and 5.00 km s^{-1}, respectively. Proceeding as previously, we find the model, typical and largest fragment size for impactors range in diameters from 1 to 100 km (see Fig. 13).

5. Conclusion

A body of laboratory work is now emerging on projectile fragmentation in impacts to rival that concerning disruption of targets. Here, basalt and shale projectiles, 1.5 mm^3 in size simulating meteorites, were fired onto water at speeds between 0.39 and 6.13 km s^{-1}. The water with the target fragments was filtered through 0.1 µm filter membrane. These were then SEM mapped and the fragments were measured using ImageJ software. A control shot was subtracted from the size distribution to account for any gun debris. Over 100,000 fragments were measured in most shots.

The ratio of the semi-major, a, to the semi-minor, b, axis was determined. The shape of the average fragment at slower speeds appear to be more circular and becomes elliptical at speeds of 1 km s^{-1} and 2 km s^{-1} onwards for basalt and shale respectively. The overall average b/a were 0.59 ± 0.16 and 0.65 ± 0.14 for basalt and shale, respectively. However, the average b/a values for fully disrupted targets, i.e. excluding the partially disrupted shots, were 0.58 ± 0.16 and 0.59 ± 0.14 for basalt and shale, respectively. This suggests that at higher speeds the morphology of basalt and shale fragments are similar. These values are however lower than for target fragments in the literature, from boulders on the surface of asteroid 25143 Itokawa, and for samples returned from Itokawa.

The cumulative fragment size distributions could not be fit by single power law functions. Instead three power laws were used in each distribution of the form $N(>S) = aS^b$, where N is the number of fragments greater than a given size S. The three S regimes were small, medium and large fragments when normalised to the original impactor size. With increasing impact speed, the gradient b of each size regime gets larger, i.e. steeper slopes. Furthermore, the behaviour of the largest fragments yields similar results to that of the fragments of catastrophically disrupted targets. That is the shapes of the size distributions for these largest fragments evolves rapidly, showing a transition from just disrupted to heavily catastrophically disrupted projectiles.

We have been able to determine the total mass survival from each shot; from this we can determine the mass survival percentage. By fitting a power law to these results we can determine how much of an impactor could survive an impact on different solar system bodies. We estimate that for basalt projectiles at typical impact speeds, there could be approximately 55%, 40%, 15% and 10% (all rounded to the nearest 5%) impactor survival at an impact site on respectively Pluto, the Moon, in the asteroid belt and Mars. Note that these are upper limits. Shale has a higher surviving mass percentage.

We considered the mass of the largest fragment-to-projectile mass ratio against the projectile energy density. For basalt we find two trends in the data, at low and high Q values, whereas for shale we find only one trend. We calculated the catastrophic disruption energy densities of basalt and shale of 24×10^4 J kg^{-1} and 9×10^4 J kg^{-1}, respectively. These results have been compared to other studies of projectile fragmentation in the literature. In general, we find the values can vary greatly depending on the target type and impact speed. However, we find they correspond to similar peak impact shock pressures (1–1.5 GPa). This is despite a range of different target types and impact speeds being used in the various experiments. The peak shock pressures in basalt at the catastrophic disruption limit, were some 4–5 times the yield strength of basalt at low strain rates. There is difference in the Q^* value found for basalt when compared to the data of Schultz and Gault (1990a), even when allowing for the differing shock pressures in the various experiments. We attribute this to the shallow angle of incidence in their work (typically less than 15°) compared to the normal incidence impacts here. At small angles it is not just the tensile strength that plays the major role in projectile breakup, with shear strength becoming important (see also Stickle and Schultz, 2011, for other examples of shear strength effects in shallow angle impacts).

We also compared our results to those for target fragmentation. Even when adjusting for size, we appear to have a larger Q^* value for projectile fragmentation than is reported for targets. The slope of the fragment cumulative size distribution appears steeper than for target fragmentation, and fragment shape also appears to differ with a lower b/a ratio.

Finally we apply a simple model based on peak shock pressure to determining information about the fate of possible impactors in many solar system impact events, with specific examples for impacts on Vesta and Ceres where we predict the fragment sizes for a wide range of impactor sizes. For the specific cases of Veneneia

and Rheasilvia craters on Vesta we find 15–25% of the impactor can survive if the impact was at the mean impact speed predicted for Vesta (around 5 km s^{-1}). This compares well with the prediction of 17% of Daly and Schultz (2016). For Ceres we find impactor retention in the typical range of 20 – 30%, somewhat higher than Daly and Schultz (2015b) where they consider basalt impacting porous snow.

Acknowledgements

We thank STFC (UK) for funding the impact laboratory at Kent. JWE thanks the University of Kent alumni for funding his Ph.D. We thank K. Harriss and N. Ramkissoon for collecting the basalt samples used in this work, J. Parnell for supplying the shale samples and Mike Cole for operating the gun. We thank the referees for useful comments and suggestions.

Supplementary materials

Supplementary material associated with this article can be found, in the online version, at doi:10.1016/j.icarus.2018.03.017.

References

A'Hearn, M.F., Belton, M.J.S., Delamere, W.A., Kissel, J., Klaasen, K.P., McFadden, L.A., Meech, K.J., Melosh, H.J., Schultz, P.H., Sunshine, J.M., Thomas, P.C., Veverka, J., Yeomans, D.K., Baca, M.W., Busko, I., Crockett, C.J., Collins, S.M., Desnoyer, M., Eberhardy, C.A., Ernst, C.M., Farnham, T.L., Feaga, L., Groussin, O., Hampton, D., Ipatov, S.I., Li, J-Y., Lindler, D., Lisse, C.M., Mastrodemos, N., Owen Jr., W.M., Richardson, J.E., Wellnitz, D.D., White, R.L., 2005. Deep impact: excavating comet Tempel 1. Science 310, 258–264.

Ahrens, T.J., Johnson, M.L.Ahrens, T.J. (Ed.), 1995. Shock wave data for rocks. Rock Physics and Phase Relations – A handbook of Physical Constants 34–44.

Armstrong, J.C., 2010. Distribution of impact locations and velocities of Earth meteorites on the Moon. Earth Moon Planets 107, 43–54.

Avdellidou, C., Price, M.C., Delbo, M., Ioannidis, P., Cole, M.J., 2016. Survival of the impactor during hypervelocity collisions – I. An analogue for low porosity targets. Mon. Not. R. Astron. Soc. 456, 2957–2965.

Avdellidou, C., Price, M.C., Delbo, M., Cole, M.J., 2017. Survival of the impactor during hypervelocity collisions – II. An analogue for high-porosity targets. Mon. Not. R. Astron. Soc. 464, 734–738.

Baldwin, E.C., Milner, D.J., Burchell, M.J., Crawford, I.A., 2007. Laboratory impacts into dry and wet sandstone with and without an overlying water layer: implications for scaling laws and projectile survivability. Meteorit. Planet. Sci. 42, 1905–1914.

Benz, W., Asphaug, E., 1999. Catastrophic disruption revisited. Icarus 142, 5–20.

Bottke, W.F., Nolan, M.C., Greenberg, R., Kolvoord, R.A., 1994. Velocity distributions among colliding asteroids. Icarus 107, 255–268.

Bowden, S.A., Court, R.W., Milner, D., Baldwin, E.C., Lindgren, P., Crawford, I.A., Parnell, J., Burchell, M.J., 2008. The thermal alteration by pyrolysis of the organic component of small projectiles of mudrock during capture at hypervelocity. J. Anal. Appl. Pyrolysis 82, 312–314.

Burchell, M.J., Cole, M.J., McDonnel, J.A.M., Zarnecki, J.C., 1999. Hypervelocity impact studies using the 2 MV Van de Graaff accelerator and two-stage light gas gun of the University of Kent at Canterbury. Meas. Sci. Technol. 10, 41–50.

Burchell, M.J., Leliwa-Kopystynski, J., Arakawa, M., 2005. Cratering of icy targets by different impactors: laboratory experiments and implications for cratering in the Solar System. Icarus 179, 274–288.

Burchell, M.J., Foster, N.J., Kearlsey, A.T., Creighton, J.A., 2008. Identification of mineral impactors in hypervelocity impact craters in aluminum by Raman spectroscopy of residues. Meteorit. Planet. Sci. 43, 135–142.

Burchell, M.J., Robin-Williams, R., Foing, B.H., 2010. The SMART-1 lunar impact. Icarus 207, 28–38.

Burchell, M.J., Cole, M.J., Price, M.C., Kearsley, A.T., 2012. Experimental investigation of impacts by solar cell secondary ejecta on silica aerogel and aluminium foil: implications for the Stardust Interstellar Dust Collector. Meteorit. Planet. Sci. 47, 671–683.

Burchell, M.J., Bowden, S.A., Cole, M., Price, M.C., Parnell, J., 2014a. Survival of organic materials in hypervelocity impacts of ice on sand, ice and water in the laboratory. Astrobiology 14, 473–485.

Burchell, M.J., McDermott, K.H., Price, M.C., 2014b. Survival of fossils under extreme shocks induced by hypervelocity impacts. Philos. Trans. R. Soc. A 372, 20130190.

Burchell, M.J., Cole, M.J., Ramkissoon, N.K., Wozniakiewicz, P.J., Price, M.C., Foing, B., 2015. SMART-1 end of life shallow regolith impact simulations. Meteorit. Planet. Sci. 50, 1436–1448.

Burchell, M.J., Harriss, K.H., Price, M.C., Yolland, L., 2017. Survival of fossilised diatoms and forams in hypervelocity impacts with peak shock pressure in the 1–19 GPa range. Icarus 290, 81–88.

Christensen N.I., Wilkens R.H., Blair S.C., and Carlson R.L. 1980. Seismic Velocities, Densities and Elastic Constants of Volcanic Breccias And Basalt From Deep Sea Drilling Project LEG 59. Initial reports of the deep sea drilling project. 515–517.

Daly, R.T., Schultz, P.H., 2013. Experimental studies into the survival and state of the projectile (abstract #2240). In: Proceedings of the 44th Lunar and Planetary Science Conference.

Daly, R.T., Schultz, P.H., 2014. How much of the impactor (and its water) ends up in Vesta's regolith? (abstract #2070). In: Proceedings of the45th Lunar and Planetary Science Conference.

Daly, R.T., Schultz, P.H., 2015a. New constraints on the delivery of impactors to icy bodies: implications for Ceres (abstract #1972). In: Proceedings of the 46th Lunar and Planetary Science Conference.

Daly, R.T., Schultz, P.H., 2015b. Predictions for impactor contamination on Ceres based on hypervelocity impact experiments. Geophys. Res. Lett. 42, 7890–7898.

Daly, R.T., Schultz, P.H., 2016. Delivering a projectile component to the vestan regolith. Icarus 264, 9–19.

Davis, D.R., Ryan, E.V., 1990. On Collisional disruption: experimental results and scaling laws. Icarus 83, 156–182.

Durda, D.D., Bottke Jr, W.F., Nesvorný, D., Enke, B.L., Merline, W.J., Asphaug, E., Richardson, D.C., 2007. Size-frequency distributions of fragments from SPH/*N*-body simulations of asteroid impacts: comparison with observed asteroid families. Icarus 186, 498–516.

Durda, D.D., Bagatin, A.C., Alemañ, R.A., Flynn, G.J., Strait, M.M., Clayton, A.N., Patmore, E.B., 2015. The shapes of fragments from catastrophic disruption events: effects of target shape and impact speed. Planet. Space Sci. 107, 77–83.

Foster, N.F., Wozniakiewicz, P.J., Price, M.C., Kearsley, A.T., Burchell, M.J., 2013. Identification of Mg–Fe content of olivine samples (by Raman Spectroscopy) after impact at 6 km s^{-1} onto aluminium foil and aerogel: in the laboratory and in wild-2 cometary samples returned by stardust. Cosmochim. Geochim. Acta 121, 1–14.

Fox, A., Snelling, P., McKenna, J., Neale, C., Neuhaus, C., Miskimmins, B., 2013. Geomechanical principles for unconventional reservoirs. MicroSeismics. MicroSeismic Inc. [online]. Available at Accessed: 12/11/2015, http://www.microseismic.com/wp-content/uploads/2017/07/2013_Geomechanical_Principles_For_Unconventional_Resources.pdf.

Fujiwara, A., Kamimoto, G., Tsukamoto, A., 1978. Expected shape distribution of asteroids obtained from laboratory impact experiments. Nature 272, 602–603.

Fujiwara, A., Cerroni, P., Davis, D.R., Ryan, E.V., Di Martino, M., Holsapple, K., Housen, K., et al., 1989. Experiments and scaling laws for catastrophic collisions. In: Binzel, R.P., et al. (Eds.), Asteroids II. University of Arizona, Tucson, pp. 240–265.

Gault, D.E., Heitowit, E.D., 1963. The partition of energy for hypervelocity impact craters formed in rock. In: Proceedings of the Sixth Hypervelocity Impact Symposium, pp. 419–456.

Gault, D.E., Wedekind, J.A., 1978. Experimental studies of oblique impact. In: Proceedingsof the 9th Lunar and Planetary Science Conference. Pergamon, New York, pp. 3843–3875.

Goderis, S., Paquay, F., Claeys, P., 2013. Projectile identification in terrestrial impact structures and ejecta material. In: Osinski, G.R., Pierazzo, E. (Eds.), Impact Cratering Processes and Products. Wiley-Blackwell, pp. 223–239. ISBN 978-1-4051-9829-5.

Harriss, K., Burchell, M.J., 2016. A study of the observed shift in the peak position of olivine Raman spectra as a result of shock induced by hypervelocity impacts. Meteorit. Planet. Sci. 51, 1289–1300.

Hayhurst, C.J., Clegg, R.A., 1997. Cylindrically symmetric SPH simulations of hypervelocity impacts on thin plates. Int. J. Impact Eng. 20, 337–348.

Hernandez, V.S., Murr, L.E., Anchondo, I.A., 2006. Experimental observations and computer simulations for metallic projectile fragmentation and impact crater development in thick metal targets. Int. J. Impact Eng. 32, 1981–1999.

Holsapple, K., Giblin, I., Housen, K., Nakamura, A., Ryan, E., et al., 2002. Asteroid impacts: laboratory experiments and scaling laws. In: Bottke, Jr., W.F., et al. (Eds.), Asteroids III. University of Arizona Press, Tucson, pp. 443–462.

Housen, K.R., Holsapple, K.A., 1999. Scale effects in strength-dominated collisions of Rocky Asteroids. Icarus 142, 21–33.

Ivanov, B.A., Melosh, H.J., 2013. Two-dimensional numerical modelling of the Rheasilvia impact formation. J. Geophys. Res.: Planets 118, 1545–1557.

Jeffers, S.V., Manley, J.P., Bailey, M.E., Asher, D.J., 2001. Near-Earth object velocity distributions and consequences for the Chicxulub impactor. Mon. Not. R. Astron. Soc. 327, 126–132.

Joy, K.H., Zolensky, M.E., Nagashima, K., Huss, G.R., Kent Ross, D., McKay, D.S., Kring, D.A., 2012. Direct detection of projectile relics from the end of the lunar basin-forming epoch. Science 336, 1426–1429.

Koncagül, E.C., Santi, P.M., 1998. Predicting the unconfined compressive strength of the Breathitt shale using slake durability, shore hardness and rock structural properties. Int. J. Rock Mech. Min. Sci. 36, 139–153.

Leliwa-Kopystynski, J., Burchell, M.J., Wlodarczy, I., 2009. The impact origin of Eunomia and Themis families. Meteorit. Planet. Sci. 44, 1929–1935.

Leliwa-Kopystyński, J., Włodarczyk, I., Burchell, M.J., 2016. Analytical model of impact disruption of satellites and asteroids. Icarus 268, 266–280.

Love, S.G., Hörz, F., Brownlee, D.E., 1993. Target porosity effects in impact cratering and collisional disruption. Icarus 105, 216–224.

Love, S.G., Ahrens, T.J., 1996. Catastrophic impacts on gravity dominated asteroids. Icarus 124, 141–155.

McDermott, K.H., Price, M.C., Cole, M., Burchell, M.J., 2016. Survivability of copper projectiles during hypervelocity impacts in porous ice: a laboratory investigation of the survivability of projectiles impacting comets or other bodies. Icarus 268, 102–117.
Melosh, H.J., 2013. The contact and compression stage of impact cratering. In: Osinski, G.R., Pierazzo, E. (Eds.), Impact Cratering: Processes and Products. Wiley-Blackwell Press, pp. 32–42. ISBN 978-1-4051-9829-5.
Michikami, T., Haegermann, A., Kadokawa, T., Yoshida, A., Shimada, A., Hasegawa, S., Tsuchiyama, A., 2016. Fragment shapes in impact experiments ranging from cratering to catastrophic disruption. Icarus 264, 316–330.
Michikami, T., Kadokawa, T., Tsuchiyama, A., Hagermann, A., Nakano, T., Uesugi, K., Hasegawa, S., 2018. Influence of petrographic textures on the shapes of impact experiment fine fragments measuring several tens of microns: Comparison with Itokawa regolith particles. Icarus 302, 109–125.
Morris, A.J.W., Burchell, M.J., 2016. Laboratory tests of catastrophic disruption of rotating bodies. Icarus 296, 91–98.
Nagaoka, H., Takasawa, S., Nakamura, A.M., Sangen, K., 2014. Degree of impactor fragmentation under collision with a regolith surface – Laboratory impact experiments of rock projectiles. Meteorit. Planet. Sci. 49, 69–79.
Nakamura, A.M., Michikami, T., Hirata, N., Fujiwara, A., Nakamura, R., Ishiguro, M., Miyamoto, H., Demura, H., Hiraoka, K., Honda, T., Honda, C., Saito, J., Hashimoto, T., Kubota, T., 2008. Impact process of boulders on the surface of asteroid 25143 Itokawa—fragments from collisional disruption. Earth Planets Space 60, 7–12.
Osinki, G.R., Pierazzo, E. (Eds.), 2013, Impact Cratering Processes and Products. Wiley-Blackwell, pp. 223–239 ISBN978-1-4051-9829-5.
Palomba, E., Longobardo, A., De Santis M. C., ZambonF., Tosi, F., Ammannito, E., Capaccioni, F., Frigeri, A., Capria, M.T., Cloutis, E.A., Jaumann, R., Combe, J-P., Raymond, C.A., Russel, C.T., 2014. Composition and mineralogy of dark material units on Vesta. Icarus 240, 58–72.
Parnell, J., Bowden, S.A., Lindgren, P., Burchell, M.J., Milner, D., Price, M.C., Baldwin, C., Crawford, I.A., 2010. The preservation of fossil biomarkers during hypervelocity impact experiments using organic rich siltstones as both projectiles and targets. Meteorit. Planet. Sci. 45, 1340–1358.
Piekutowski, A.J., 1995. Fragmentation of a sphere initiated by hypervelocity impact with a thin sheet. Int. J. Impact Eng. 17 (4), 627–638.
Price, M.C., Kearsley, A.T., Burchell, M.J., Hörz, F., Borg, J., Bridges, J.C., Cole, M.J., Floss, C., Graham, G., Green, S.F., Hoppe, P., Leroux, H., Marhas, K.K., Park, N., Stroud, R., Stadermann, F.J., Telisch, N., Wozniakiewicz, P.J., 2010. Comet 81P/Wild 2: the size distribution of finer (sub-10 μm) dust collected by the Stardust spacecraft. Meteorit. Planet. Sci. 45, 1409–1428.
Price, M.C., Kearsley, A.T., Burchell, M.J., Howard, L.E., Hillier, J.K., Starkey, N.A., Wozniakiewicz, P.J., Cole, M.J., 2012. Stardust dust calibration: hydrocode modelling of impacts on Al-1100 foil at velocities up to 300 km s^{-1} and validation with experimental data. Meteorit. Planet. Sci. 47 (4), 684–695.
Price, M.C., Kearsley, A.T., Burchell, M.J., 2013. Validation of the Preston-Tonks-Wallace strength model at strain rates approaching 10^{11} s^{-1} for Al-1100, tantalum and copper using hypervelocity impact crater morphologies. Int. J. Impact Eng. 52, 1–10.
Reddy, V., Le Corre L., O'BrienD.P., Nathues, A., Cloutis, E.A., Durda, D.D., Bottke, W.F., Bhatt, M.U., Nesvorny, D., Buczkowski, D., Scully, J.E.C., Palmer, E.M., Sierks, H., Mann, P.J., Becker, K.J., Beck, A.W., Mittlefehldtj, D., Li, J-Y., Gaskell, R., Russell, C.T., Gaffey, M.J., McSween, H.Y., McCord, T.B., Combe, J-P., Blewett, D., 2012. Delivery of dark material to Vesta via carbonaceous chondritic impacts. Icarus 221, 544–559.
Rocchi, V., Sammonds, P.R., Kilburn, C.R.J., 2002. Flow and fracture maps for basaltic rock deformation at high temperatures. J. Volcanol. Geotherm. Res. 120, 25–42.
Ryan, E.V., 2000. Asteroid fragmentation and evolution of asteroids. Ann. Rev. Earth Planet. Sci. 28, 367–389.
Schenk, P., O'Brien, D.P., Marchi, S., Gaskell, R., Preusker, F., Roatsch, T., Jaumann, R., Buczkowski, D., McCord, T., McSween, H.Y., Williams, D., Yingst, A., Raymond, C., Russell, C., 2012. The geologically recent giant impact Basins at Vesta's South Pole. Science 336, 694–697.
Schultz, P.H., Gault, D.E., 1984. Effects of projectile deformation on crater efficiency and morphology. In: Proceedings of the 15th Lunar and Planetary Science Conference.
Schultz, P.H., Gault, D.E., 1990a. Prolonged Global Catastrophes from Oblique Impacts.. Geological Society of America, pp. 239–261. Special Paper 247.
Schultz, P.H., Gault, D.E., 1990b. Decapitated impactors in the laboratory and on the planets. In: Proceedings of the 21st Lunar and Planetary Science Conference, pp. 1099–1100.
Schultz, P.H., Hermalyn, B., Veverka, J., 2013. The deep impact crater on 9P/Tempel-1 from Stardust-NExT. Icarus 222, 502–515.
Schultz, P.H., Crawford, D.A., 2016. Origin and implications of non-radial Imbrium Sculpture on the Moon. Nature 535 (7612), 391–394.
Schultz, R.A., 1993. Brittle strength of basaltic rock masses with applications to Venus. J. Geophys. Res. Planets 98, 10883–10895.
Steel, D., 1998. Distribution and moments of asteroid and comet impact speeds upon the Earth and Mars. Planet. Space Sci. 46, 473–478.
Stickle, A.M., Schultz, P.H., 2011. Exploring the role of shear in oblique impacts: a comparison of experimental and numerical results for planar targets. Int. J. Impact Eng. 38, 527–534.
Stickle, A.M., Schultz, P.H., Crawford, D., 2015. Subsurface failure in spherical bodies: a formation scenario for linear troughs on Vesta's surface. Icarus 247, 18–34.
Takagi, Y., Mizutani, H., Kawakami, S.I., 1984. Impact fragmentation experiments of basalt and prophyllites. Icarus 59, 462–477.
Tsuchiyama, A., Uesugi, M., Uesugi, K., Nakano, T., Noguchi, R., Matsumoto, T., Matsuno, J., Nagano, T., Imai, Y., Shimada, A., Takeuchi, A., Suzuki, Y., Nakamura, T., Noguchi, T., Abe, M., Yada, T., Fujimura, A., 2014. Three-dimensional microstructure of samples recovered from asteroid 25143 Itokawa: comparison with LL5 and LL6 chondrite particles. Meteorit. Planet. Sci. 49, 172–187.
Veverka, J., Klaasen, K., A'Hearn, M., Belton, M., Brownlee, D., Chesley, S., Clark, B., Economou, T., Farquhar, R., Green, S.F., Groussin, O., Harris, A., Kissel, J., Li, J-Y., Meech, K., Melosh, J., Richardson, J., Schultz, P., Silen, J., Sunshine, J., Thomas, P., Bhaskaran, S., Bodewits, D., Carcich, B., Cheuvront, A., Farnham, T., Sackett, S., Wellnitz, D., Wolf, A., 2013. Return to Comet Tempel 1: overview of Stardust-Next results. Icarus 222, 424–435.
Yue, Z., Johnson, B.C., Minton, D.A., Melosh, H.J., Di, K., Hu, W., Liu, Y., 2013. Projectile remnants in central peaks of lunar impact crater. Nat. Geosci. 6, 435–437.
Zahnle, K., Schenk, P., Levison, H., Dones, L., 2003. Cratering rates in the outer Solar System. Icarus 163, 263–289.